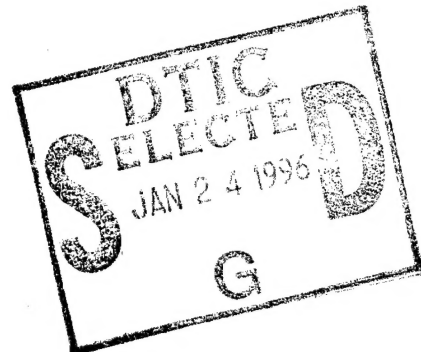


cm



CCM-82-10

FRACTURE BEHAVIOR OF COLLIMATED
THERMOPLASTIC POLY(ETHYLENE
TEREPHTHALATE) REINFORCED WITH
SHORT E-GLASS FIBER

C. LHYMN

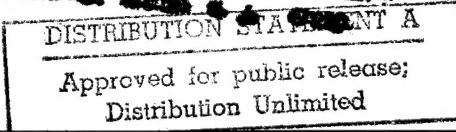
J. M. SCHULTZ

19951226 060

CENTER FOR COMPOSITE MATERIALS

College of Engineering
University of Delaware
Newark, Delaware

DTIG QUALITY INSPECTED



LASTEC

Date: 7/11/95 Time: 6:37:16PM

Page: 1 Document Name: untitled

DTIC DOES NOT HAVE THIS ITEM

-- 1 - AD NUMBER: D437148
-- 5 - CORPORATE AUTHOR: DELAWARE UNIV NEWARK CENTER FOR COMPOSITE MATERIALS
-- 6 - UNCLASSIFIED TITLE: FRACTURE BEHAVIOR OF COLLIMATED THERMOPLASTIC POLY(ETHYLENE TEREPHTHALATE) REINFORCED WITH SHORT E-GLASS FIBER.
--10 - PERSONAL AUTHORS: LHYNM,C. ;SCHULTZ,J. M. ;
--11 - REPORT DATE: JUL , 1982
--12 - PAGINATION: 75P
--14 - REPORT NUMBER: CCM-82-10
--20 - REPORT CLASSIFICATION: UNCLASSIFIED
--22 - LIMITATIONS (ALPHA): APPROVED FOR PUBLIC RELEASE; DISTRIBUTION UNLIMITED. AVAILABILITY: CENTER FOR COMPOSITE MATERIALS, UNIVERSITY OF DELAWARE, NEWARK, DE 19711.
--33 - LIMITATION CODES: 1 24

FRACTURE BEHAVIOR OF COLLIMATED
THERMOPLASTIC POLY(ETHYLENE TEREPHTHALATE)
REINFORCED WITH SHORT E-GLASS FIBER

C. Lhymn

J. M. Schultz

Center for Composite Materials
University of Delaware
Newark, Delaware

Accesion For	
NTIS	CRA&I <input checked="" type="checkbox"/>
DTIC	TAB <input type="checkbox"/>
Unannounced <input type="checkbox"/>	
Justification _____	
By _____	
Distribution / _____	
Availability Codes	
Dist	Avail and/or Special
A-1	

Sponsored by the
University-Industry Research Program
"Application of Composite Materials
to Industrial Products"

July 1982

DISTRIBUTION STATEMENT A
Approved for public release;
Distribution Unlimited

ABSTRACT

The fracture behavior of thermoplastic poly(ethylene terephthalate) reinforced with short E-glass fiber was investigated, using fractography and a fracture mechanics approach. The observed microstructures, crack propagation, and the stress-rupture lifetime data indicate a sudden breakdown induced by far-field effects. The critical damage appears to be correlated with a ductile-to-brittle transition of matrix fracture. The calculation of fracture toughness for various fiber orientations indicates that the fiber pull-out energy is the dominant term in the case in which the fiber orientation is perpendicular to the notch tip.

TABLE OF CONTENTS

Acknowledgments	iv
Introduction	1
Experimental	3
Results	11
A. Crack Propagation	11
B. Matrix Fracture Morphology	28
C. Stress-Rupture Lifetime	37
D. Tensile Testing and K_c Measurement	41
Discussion	44
A. Fractographic Model	44
B. Microscopic/Macroscopic Correlation	52
Conclusions	57
References	60
Appendix	62

ACKNOWLEDGMENTS

The authors are particularly grateful to Drs. E. Deyrup and B. Epstein of E. I. du Pont de Nemours and Company for supplying injection molded Rynite ® plaques, for useful consultation, and for their general support of this work.

INTRODUCTION

Composite injection-molding compounds consist of short fibers dispersed in a thermoplastic matrix. Injection-molding compounds have an advantage over short-fiber sheet-molding compounds (thermosetting matrix) and continuous fiber systems because of the possibility of molding complex shapes. Principal disadvantages are the relatively soft matrix and a present lack of predictability of the ultimate properties. Of primary concern in the ultimate mechanical behavior is the orientation distribution of and interactions among the fibers.

All previous work on injection-molding compounds has utilized as-molded material. Such material is extremely inhomogeneous, exhibiting surface layers in which fibers are oriented in the mold-fill direction (MFD) and a core in which the fibers are preferentially aligned normal to the MFD [1-4]. In such a circumstance, it is difficult to study mechanisms of failure, because of the added complications of the orientation inhomogeneity. In the present study, single-ply material has been used and failure behavior has been followed.

Both fractography and linear elastic fracture mechanisms (LEFM) have been used to characterize failure.

With regard to the use of LEFM, this approach has been found of general utility in composite fracture work [5-13], and its utility in characterizing failure in short-fiber composites has recently been demonstrated [1-3, 14].

Recent study of polyamide thermoplastic reinforced with short glass and graphite fibers [15] demonstrated that the failure is likely to initiate at fiber ends. The proposed damage model [16] implies specimen breakdown in a critical cross section that has been weakened by the accumulation of cracks. The above model of a bridging zone was approached using probability theory, assuming that the failure of the composite occurs due to the inability of the short fibers bridging a critical zone to carry the load [17].

The present work will reveal the topological model of sudden breakdown based on a far-field effect. Also, the concept of a critical crack length will be introduced to explain the ductile-to-brittle transition in fracture mode with respect to a sudden catastrophic failure.

EXPERIMENTAL

Rynite [®] 545, an injection molding compound, consisting of a thermoplastic poly(ethylene terephthalate) (PET) matrix filled with approximately 45 weight percent chopped E-glass fibers, was used throughout this work. The diameter of the fiber is 12 μm . The material was injection molded into 5" \times 7" \times 1/8" (12.7 cm \times 17.8 cm \times 0.32 cm) plaques, using an end-gated mold. It has recently been shown, for this material, that the fiber orientation varies systematically across the specimen thickness [1-3]. Near the mold surface, the fibers are aligned in the mold-fill direction (MFD); in the center section, distant from the surface, the fibers are oriented in the plane of the plaque and approximately normal to the MFD.

A fracture plane containing the thickness direction and the normal to the MFD is shown in Figure 1. The two surface layers and the orthogonally oriented core are easily seen. To obtain a single layer ply, the as-molded three-layer laminate is machined from one side only to 1/3 of the initial thickness. This process effectively eliminates one outer layer and the "core."

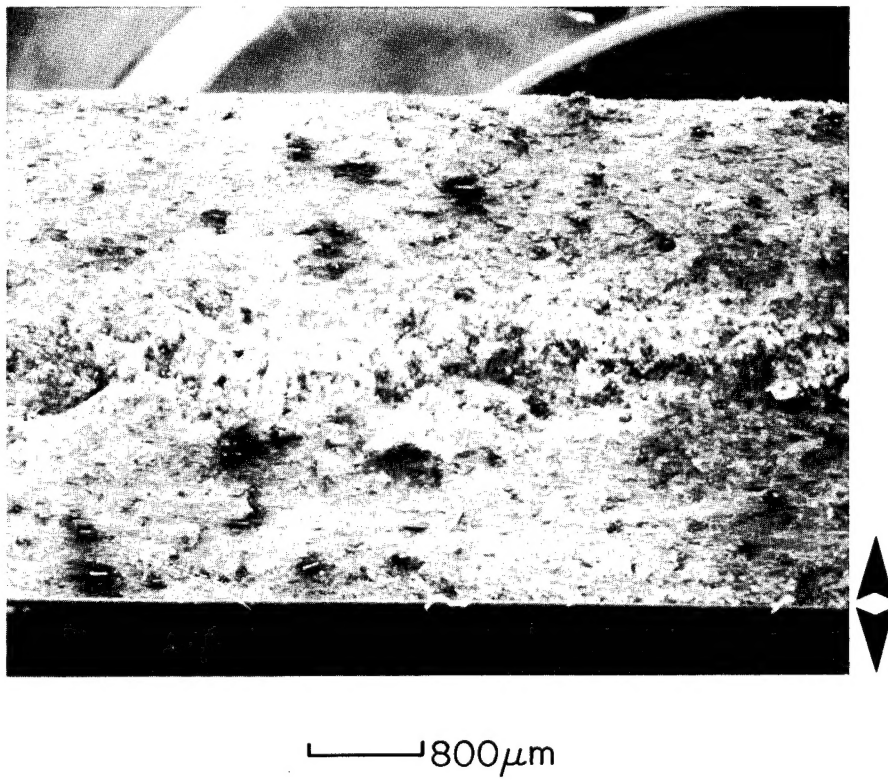


Figure 1. Fiber distribution along the thickness (1/8 inch) direction (↔). The MFD is perpendicular to the plane of the paper. This is a natural three-layer laminate caused by the process of injection molding.

Compact tension specimens are used in this work.

The specimen dimensions are shown in Figure 2. These dimensions are smaller than those specified by ASTM E399-74. Two reasons why the reduced size is chosen are:

- 1) Elimination of instability-related shear fracture mode. This problem plagued the early phases of this work, but was finally obviated by the relatively short geometry of Figure 2, and also by the use of lateral constraints.
- 2) Reduction of specimen warpage.

Three kinds of machine-notch geometry are used: L-specimen ($\theta = 90^\circ$), 45° -specimen ($\theta = 45^\circ$), and T-specimen ($\theta = 0^\circ$).

Here, θ denotes the angle between MFD and notch.

For thin specimens (0.10 cm on average), it was found impossible to maintain the planar shape the sample when the load is high (instability). The phenomenon of instability is illustrated in Figure 3. When such instability develops, the crack propagation and final fracture mode become shear-like. Such an instability was eliminated by decreasing the notch-crack distance, a , so that mode I fracture was accomplished instead of mode III in case of L-specimens.

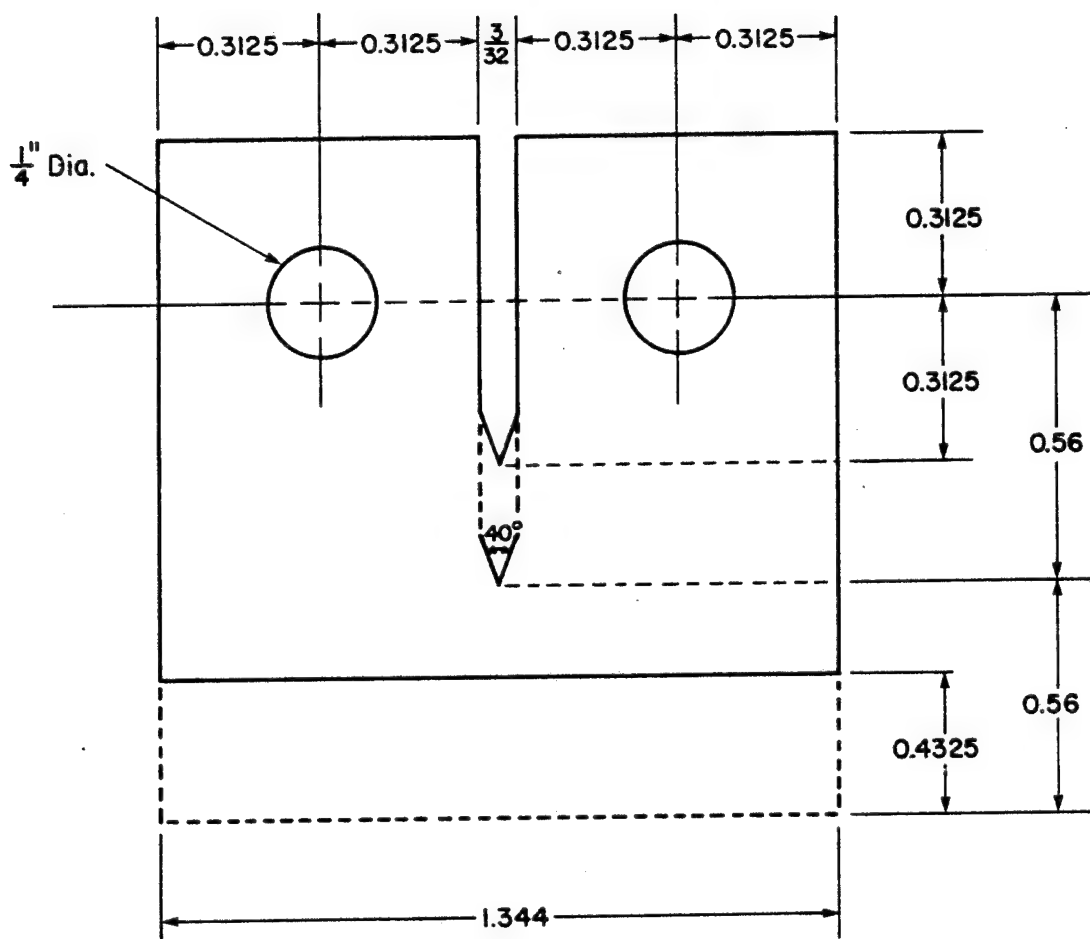


Figure 2. Geometry of compact tension specimen.
(Extended dotted line size is the reduced
version of ASTM designation: E399-74.)

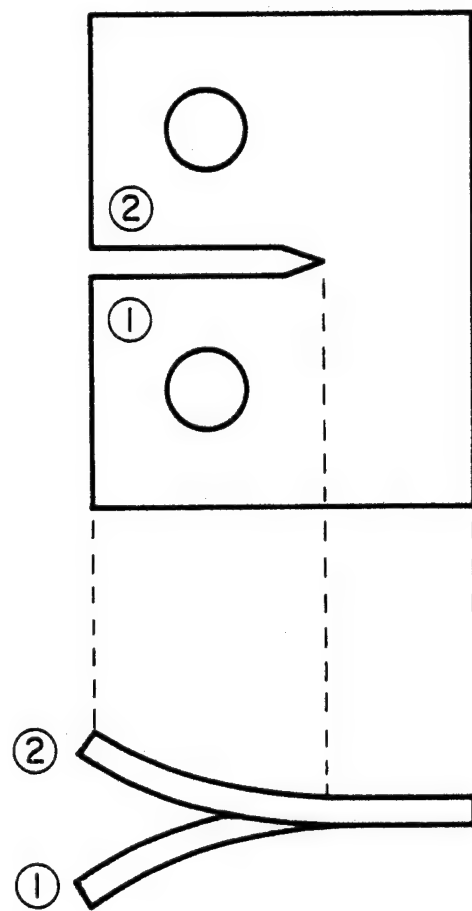


Figure 3. The mode of instability. When the load becomes high, the thin sheet specimen (0.10 cm thick) takes the position indicated in the top view.

Specifically modified metal side support plates [18] were employed also to inhibit mode III shear fracture. But it was discovered that this metal fixture could not prevent shear fracture always, because, when the shear stress becomes extremely high, the metal fixture itself could not maintain the planar shape. It is only effective under a low shear stress acting on the sample.

The as-injection-molded, rectangular plaque warps during the machining to about 1/24-inch thickness, probably due to internal stresses. Typical warpage is 5 mm over a 12.5 cm length.

Tensile specimens used for constant strain rate tensile testing are of dog-bone geometry, with a 9.53 mm gage length, radii of 12.7 mm radius and a 3.18 mm \times 3.18 mm cross-section.

Static stress-rupture experiments are economically instrumented as illustrated in Figure 4. Here a specimen failure trips a switch (s_n) from the normal a_n connection to b_n connection, which changes the input voltage to a strip chart recorder. The pen motion on the recorder indicates both which specimen has failed and when. The switch is normally connected to position a_n ($n = 1, 2, \dots, n$) but, when the specimen is fractured completely, is connected to position

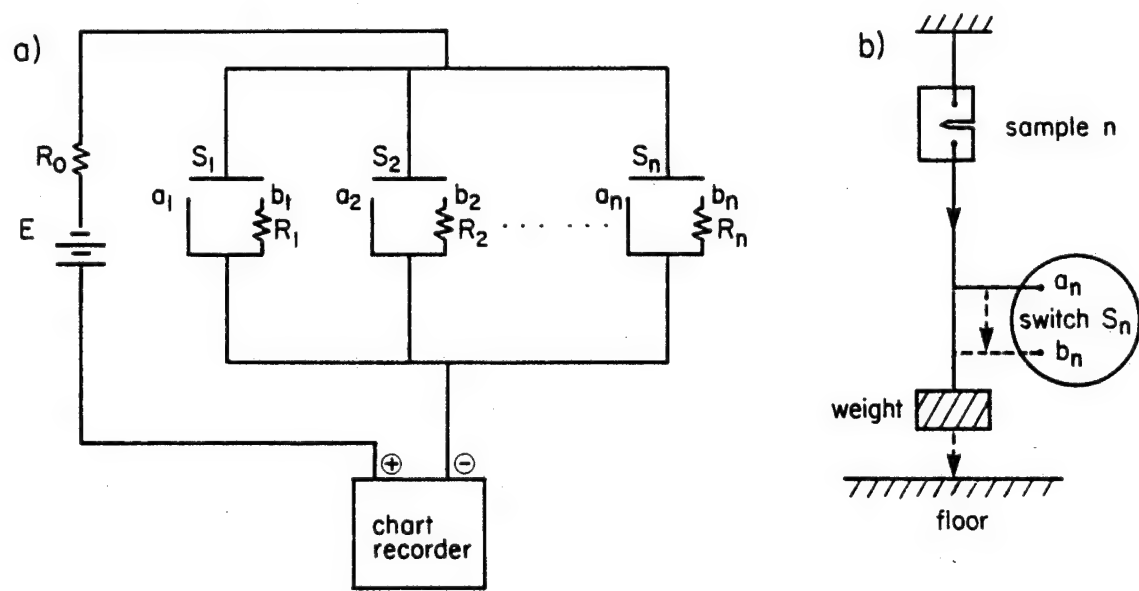


Figure 4. Instrumentation for economical stress-rupture test of many specimens.

- (a) Electronics
- (b) Mechanical: dotted line is the case of specimen breakdown.

b_n by the mechanical process shown in Figure 10-(b).

Different values of R_n cause a different step height in a time-based chart recording signal.

RESULTS

A. Crack Propagation

1) Crack Propagation of L-Specimens Under Static Loading

The typical behavior for crack propagation under an air environment is as follows. Under an initially applied load, the crack grows to a certain length and then further growth is virtually stopped (crack arrest). When the load is increased a little, the crack propagates suddenly to fracture after a certain duration of holding time. The stage of classical crack acceleration [19] was impossible to detect, due to the instantaneous failure. The initial stage of crack growth is discontinuous, the crack propagating in a step-wise fashion, as illustrated in Figure 5.

Crack propagation has been followed by microscopic examination of the surfaces of the compact tensile specimens. Figure 6 shows optical micrographs of the early stages of crack propagation. Figure 7 is a scanning electron micrograph from the vicinity of the tip of a growing crack. As can be seen, scanning electron microscopy is especially sensitive to small fractures, since those fissures are not accessible

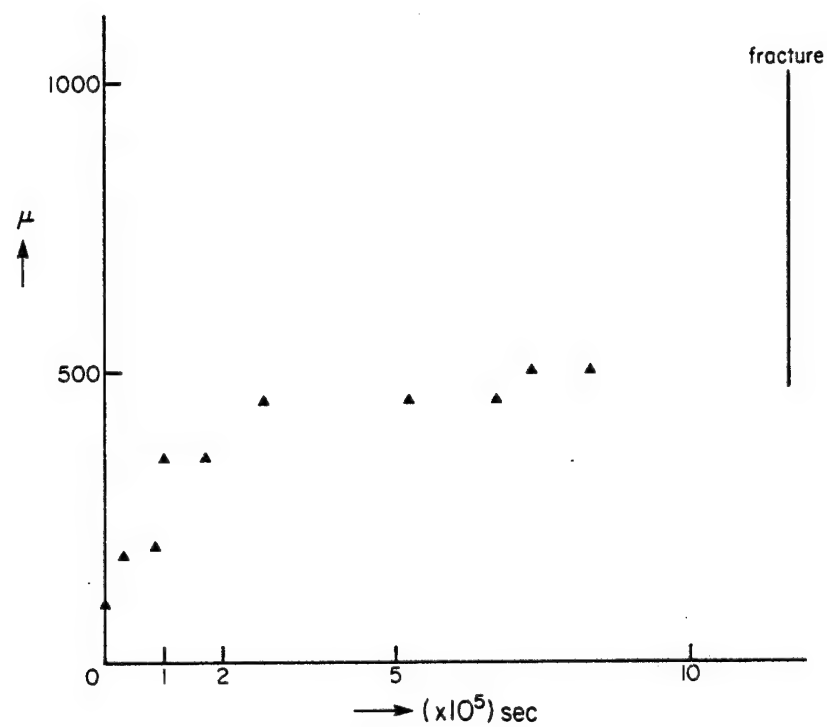


Figure 5. Static crack growth of L-specimen under a constant load (12.9 kg.).

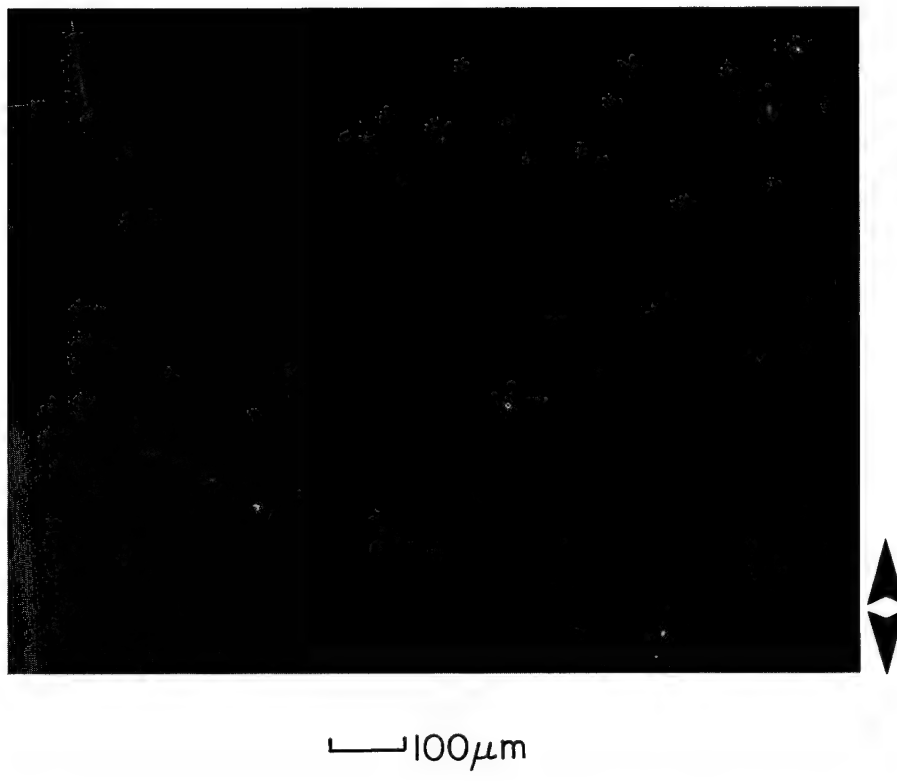


Figure 6. Optical micrographs showing early stages in the propagation of a crack in an L-oriented compact tensile specimen.

(a) Constant load: (9.08 kg.). The black arc at the far left center is the tip of a machined-notch crack. Generally, the crack propagates through the matrix and the matrix-fiber interface.

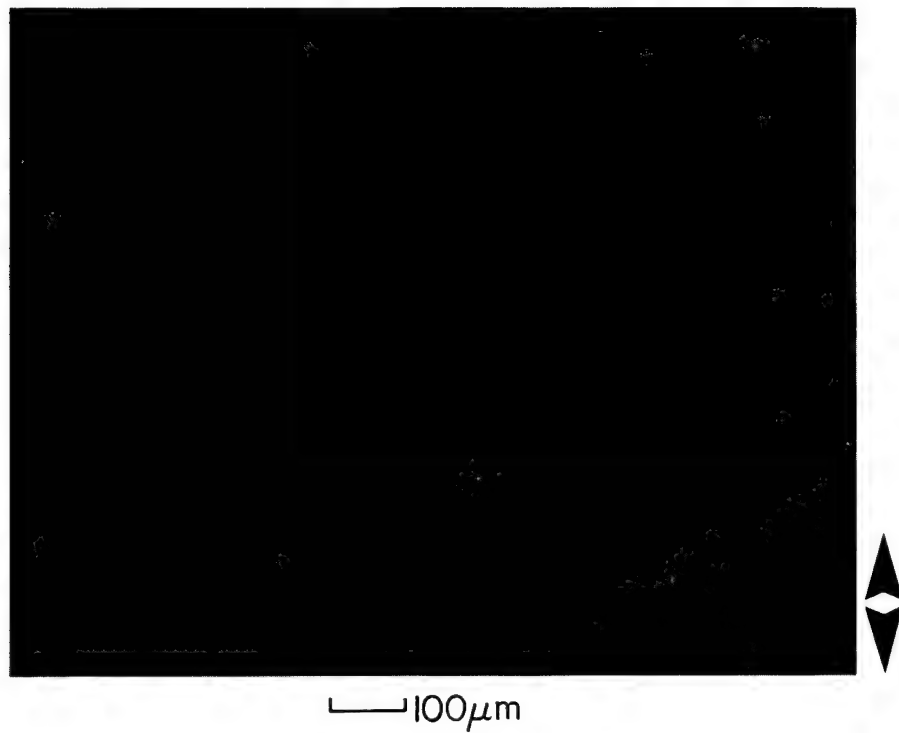


Figure 6. (b) Same as (a), but later. First arrow indicates interfacial debonding and second arrow indicates fiber fracture.

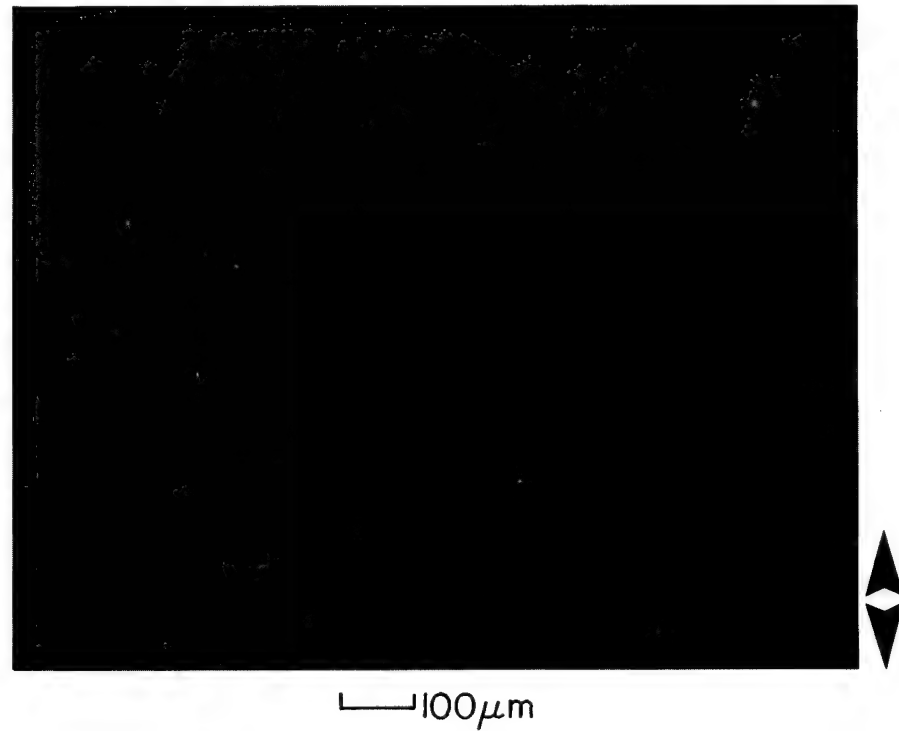


Figure 6. (c) Constant load increased to 9.67 kg. The arrow indicates matrix cracking.

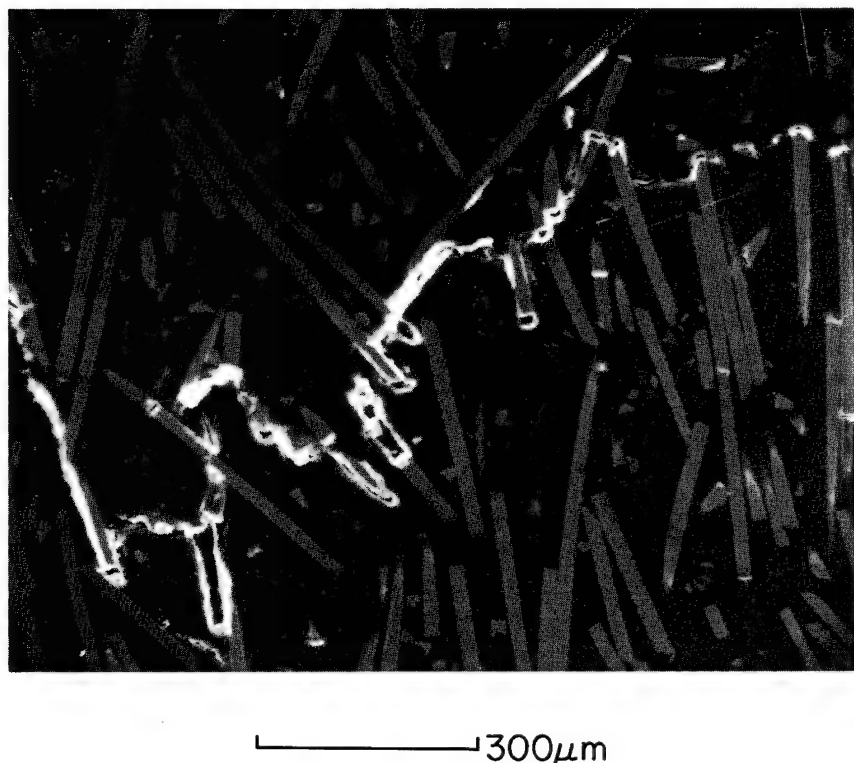


Figure 7. SEM view along a crack path.

to the evaporated gold coating and consequently act as sites of electrostatic charging.

These micrographs are typical of what is observed.

A summary of the observation is:

- 1) The crack path has an irregular, zig-zag shape, but propagates along the center line, on average.
- 2) Microcracks develop at the fiber ends. The voiding of a fiber end is shown at larger magnification in Figure 8. The detachment of matrix at the interface results in the formation of microcracks, which finally coalesce to form a continuous crack under the necking and yielding of the crazed matrix between them. The coalescence has formed a continuous yielded zone, which is torn apart, leaving individual dimples of stretched matrix material.
- 3) Interfacial debonding follows the fiber-end microcracking.
- 4) A large degree of fiber fracture is observed. This fiber fracture is induced by the combined action of tensile stress and shear stress. The shear stress from the neighboring fiber tip is

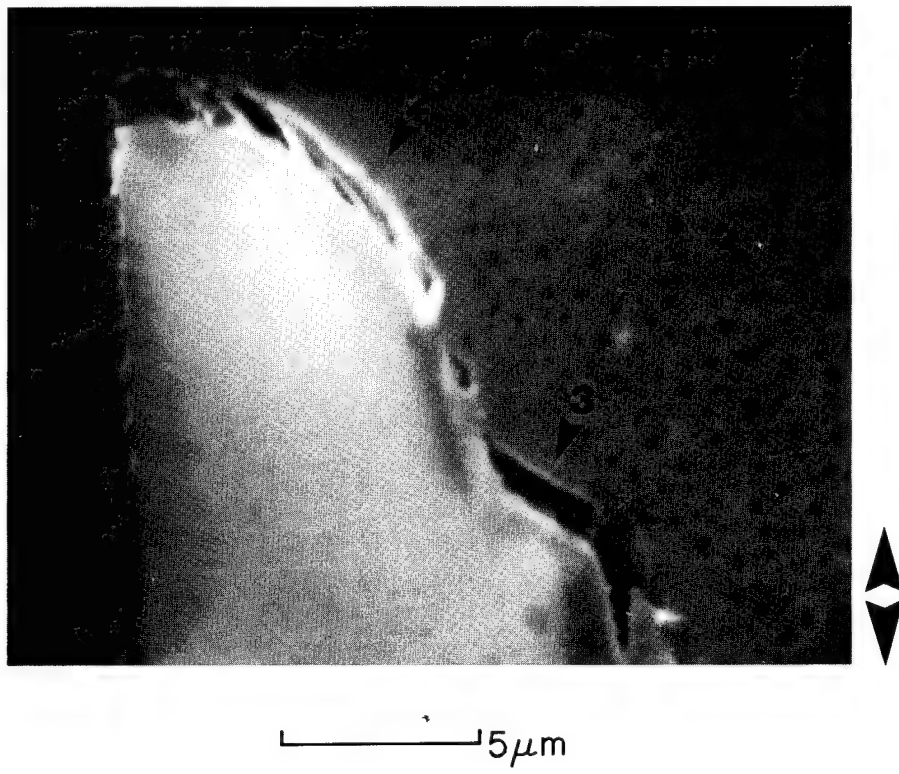


Figure 8. Voiding, crazing and microcracking at fiber end. First arrow indicates void formation under shear stress; second arrow indicates crazed matrix; third arrow indicates detached matrix-induced microcracks. (18.25 kg. vertical loading.)

transferred through the matrix. There appears to be a critical distance, above which the shear stress is not effective in inducing a fiber fracture. The net result of the interaction of a neighboring fiber end is the increased tensile force on the surface of the adjacent fiber.

- 5) Generally, the fiber fracture is accomplished long before the general crack tip arrives.

When the crack tip meets a fiber which is not fractured previously, interface debonding and fiber pull-out is the mechanism of crack propagation.

- 2) Crack Propagation of T-Specimens Under Static Loading

Crack propagation data for two T-specimens are shown shown in Figure 9. There is a step-wise crack growth; however, this behavior is diminished with respect to L-oriented specimens.

A typical crack tip micrograph is shown in Figure 10. The fracture mechanism is mainly interface debonding plus matrix cracking, a critical process being the matrix crazing

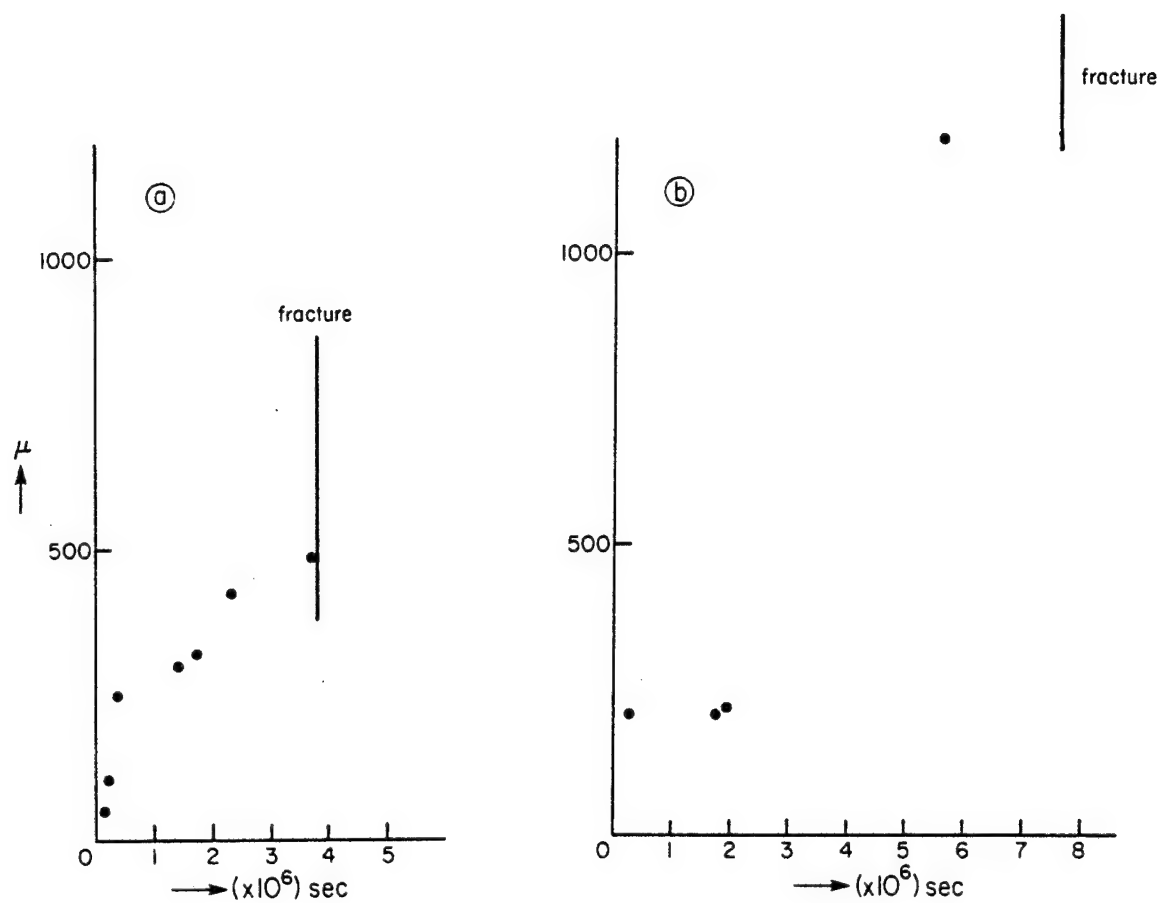


Figure 9. Static crack propagation of T-specimens (a) and (b).

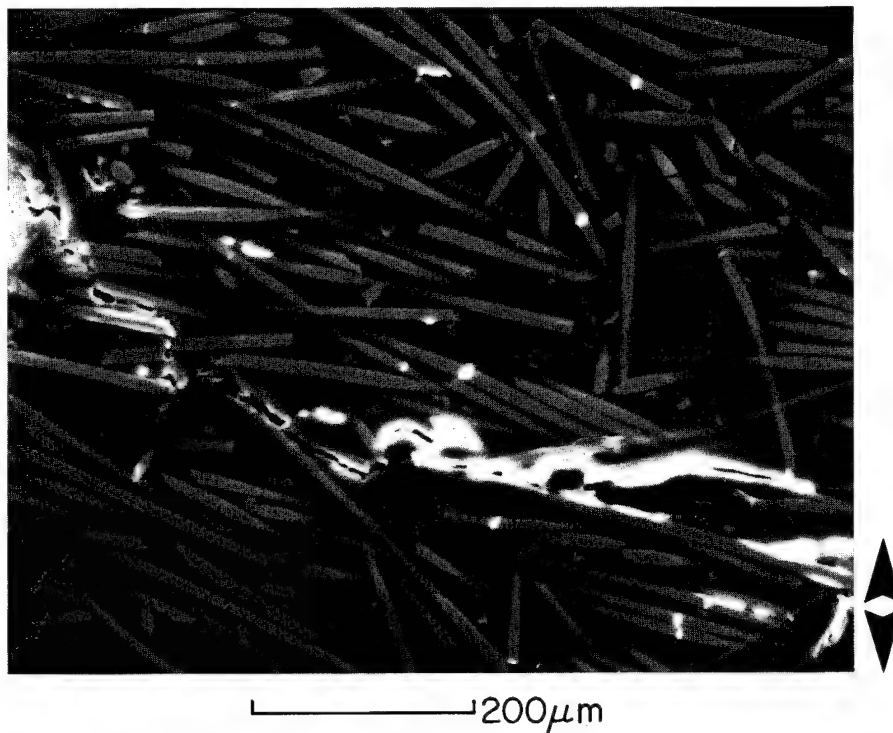


Figure 10. (a) Crack propagation from the notch tip (far left arc) is mainly along the interface in the case of the T-specimen. Matrix crazing is the joining mechanism of pre-existing interface cracks.

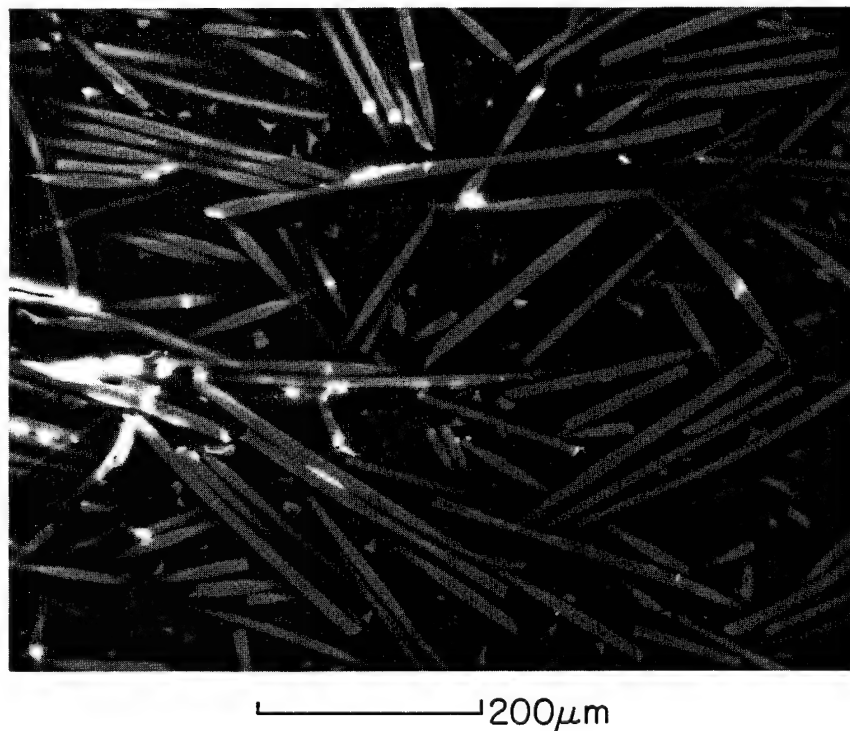


Figure 10. (b) Crack tip area of (a). Fiber fracture and interface debonding are accomplished far away from the main crack tip (10 kg. loading).

to join microcracks. That is, the interface failure is seen far ahead of the front of the continuous crack; joining-up is the only remaining obstacle. Fiber fracture is still visible, but its role is minor.

Matrix cracking is believed to be preceded by crazing. (Molecules become oriented in fibrils at a small angle to the stress axis.) Individual crazes increase in density with increasing load time until they coalesce to form a continuous band of yielding and necking. This zone later tears apart, at first at individual holes, to form a continuously cracked plane.

3) Crack Propagation of 45°-Specimens Under Static Loading

Crack propagation data for a specimen with fibers at 45° to the tensile axis is shown in Figure 11. Again, the crack propagation is discontinuous, but much less so than for L-specimens.

Figure 12 is typical of the crack morphology seen in this orientation. The following points can be drawn:

- 1) The crack grows along the fiber axis.
- 2) Several cracks grow concurrently and the topological connection of such branches is

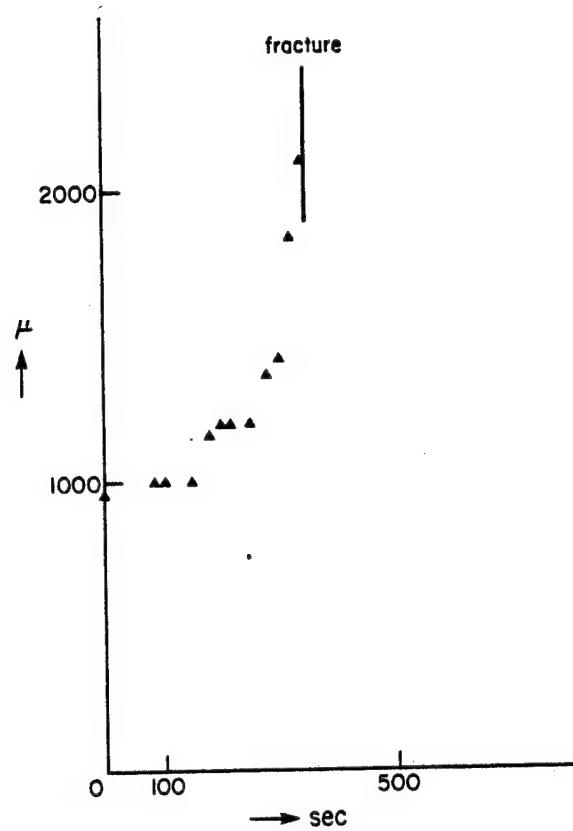


Figure 11. Static crack propagation of 45°-specimen under 7.45 kg. load.

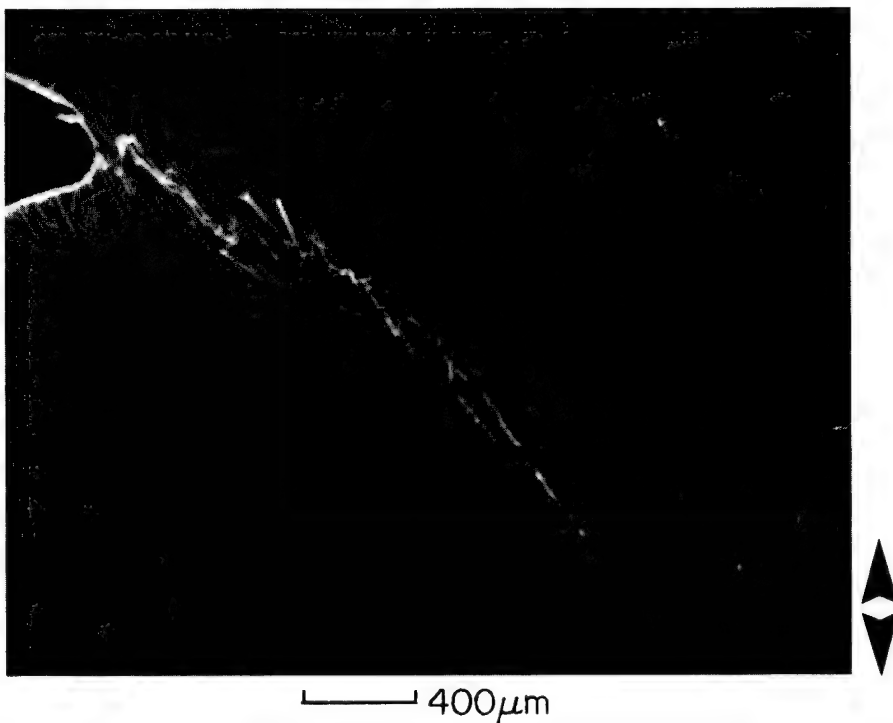


Figure 12. (a) Static crack growth in 45°-specimen. Crack follows the fiber orientation. Several crack branches propagate simultaneously. The connectivity of such branches is the criterion of ultimate failure (10 kg. loading).

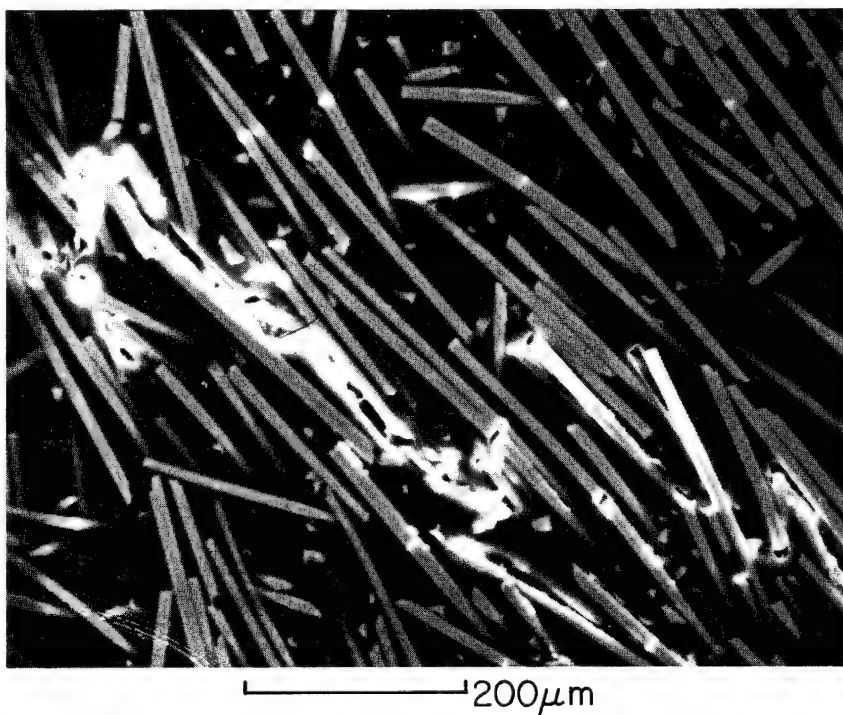


Figure 12. (b) Same as (a) but magnified. Interface debonding is believed to develop through shear stress-induced voiding, cracking and crazing. Fiber fractures are visible away from the crack tip (far-field effect).

the growth process of the main crack tip

- 3) A matrix crack grows by a crazing process, as shown in Figure 13.
- 4) The role of fiber fracture is less significant than it is for the L-geometry

4) Fatigue Crack Propagation

Crack propagation data for L- and T-specimens are given in Figures 14 and 15. The shape of the crack propagation curve for 45° material is similar. Two features are evident:

- 1) The crack velocity is quite constant; i.e., a quasi-linear behavior of a vs. N relationship is observed. Plotting da/dN vs. ΔK_I , the curve fluctuates about a constant level.
- 2) Discontinuous crack growth is again seen.

A series of micrographs were taken during interruption of a tension-tension sinusoidal load-control fatigue experiment (5 Hz, max. load = 10 kg, $R = 0.22$) of an L-specimen. Excerpts from that series are given in Reference [18]. It is clear that the crack propagates by interface debonding and ultimate pull-out, plus matrix cracking. Fiber fracture is observed

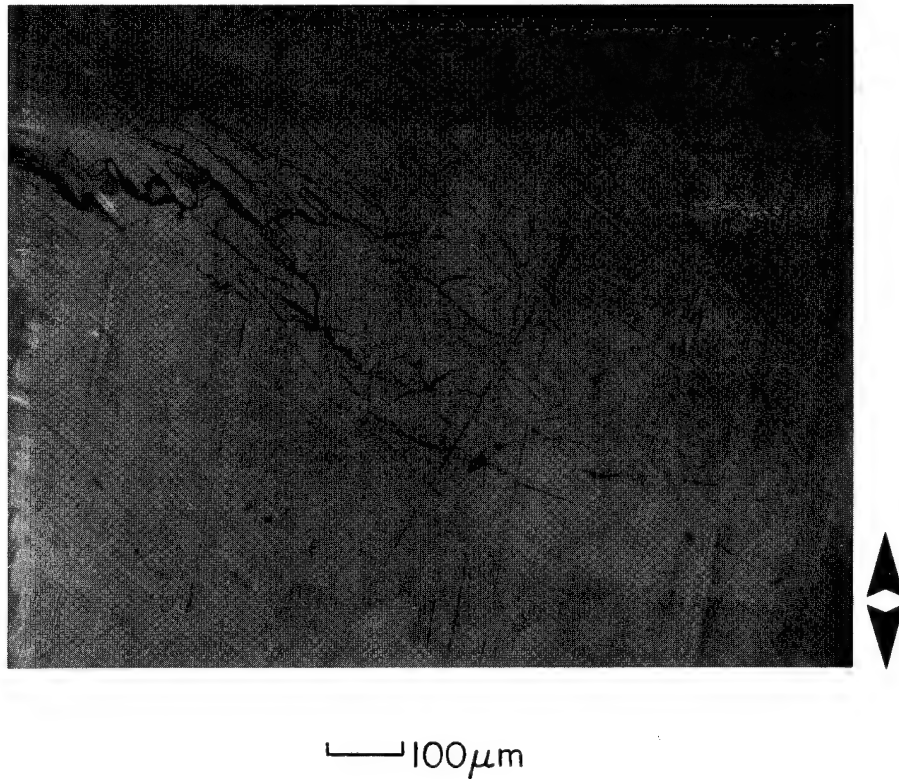


Figure 13. Optical micrograph of 45°-specimen. Enhanced matrix crazing at localized places is one evidence of a far-field effect (7.45 kg. loading).

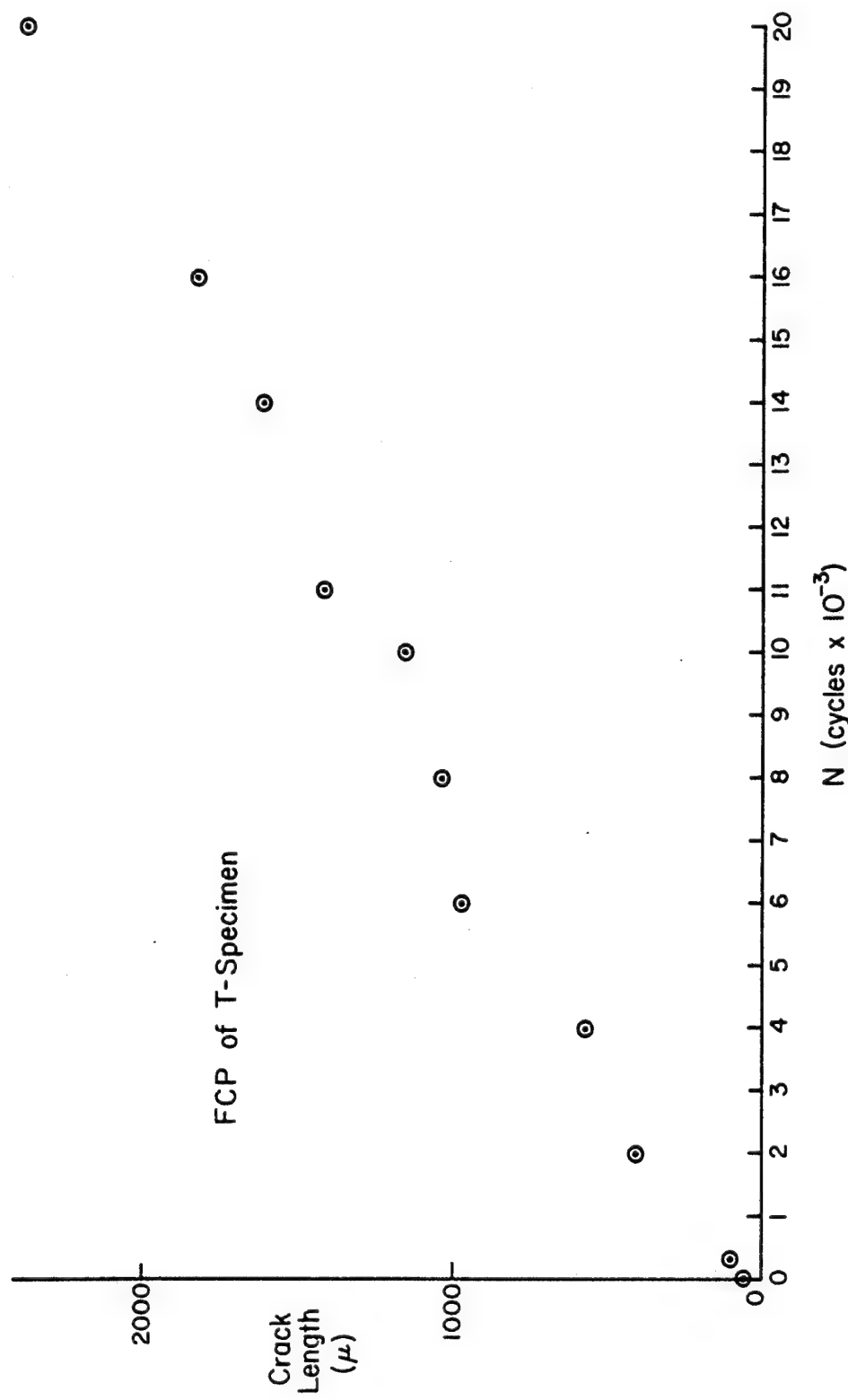


Figure 14. Fatigue crack propagation of L-specimen.

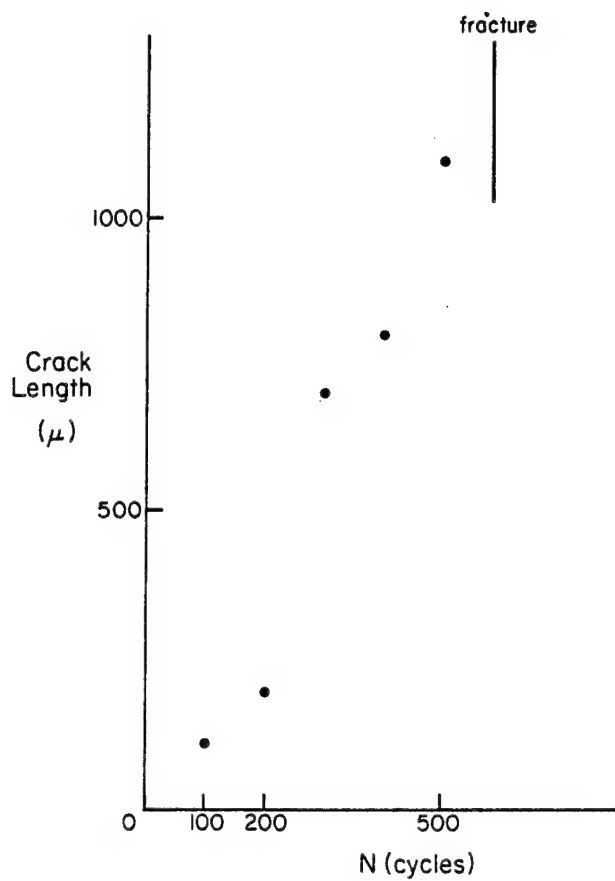


Figure 15. Fatigue crack propagation of T-specimen
($R = 0.22$, 9 kg. maximum).

only in the far field, never near the main crack tip. Again, the connecting of far-field microcracks is critical to the failure process.

A recent study on fatigue crack propagation in graphite-fiber-reinforced (discontinuous fiber) Nylon 66 [20] reports a constant flaw propagation rate for almost the whole life except only in the last few cycles of crack acceleration. The mechanism proposed was that the damaged zone around the flaw tip grows linearly with time until the material has been weakened enough to cause rapid failure. The present study indicates the same linear growth behavior, but the connectivity of several discrete microcracks is a new consideration.

B. Matrix Fracture Morphology

The examination of fracture surfaces is useful in providing information regarding mechanisms of failure. As was pointed out above, fiber fracture or debonding can occur well ahead of the general crack. Connectivity of such far-field microcracks, through matrix deformation and failure, is necessary to crack propagation. The fracture surface contains information on the failure history of the matrix and is examined here in that context.

1) Stress-Rupture

The stress-rupture test is a constant loading situation and there is no limit on strain rate. Initially, the stress is concentrated near the notch tip and a crack grows slowly. But as the crack length increases, the stress concentration factor increases and then finally crack instability induces a fast (instantaneous) crack propagation. As we have seen, the three-dimensional fracture surface of an L-specimen shows a zig-zag shape, while that of a T-specimen shows a flat fracture surface.

Examination of the matrix for the L-orientation shows a ductile-to-brittle transition along the fracture surface. An example is shown in Figure 16. Here the matrix near the machine notch shows ductile fracture; the material toward the opposite end shows brittle fracture. The transition occurs at about 3,000 μm (values for the three L-specimens measured were 3700, 2800, and 2800 μm).

The following observations derive from the fracture surface micrography:

- 1) There is a ductile-to-brittle transition from the notch tip to the specimen end.

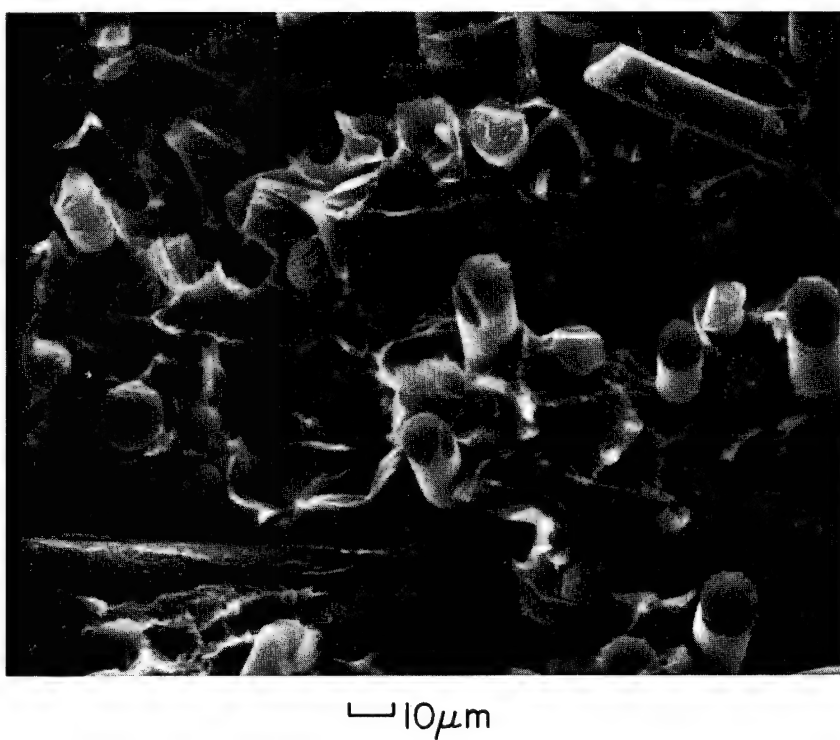


Figure 16. (a) Ductile zone (slow crack propagation) of L-specimen near notch.

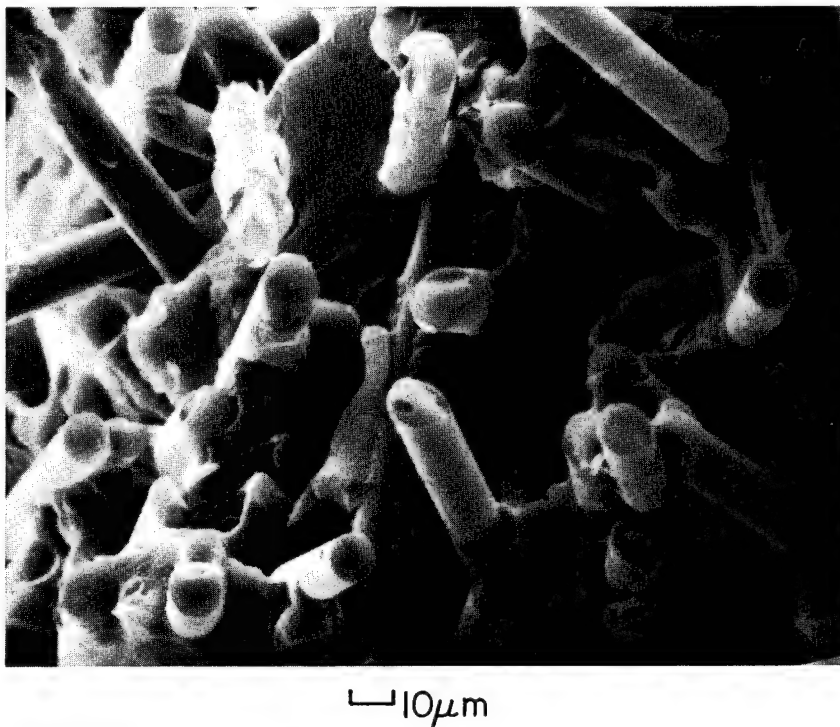
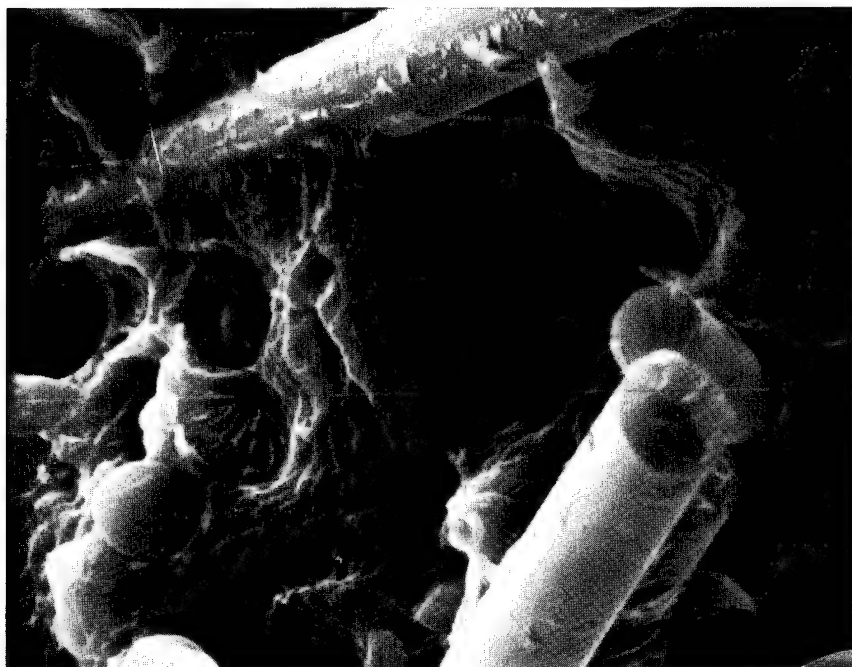


Figure 16. (b) End section: brittle matrix failure.

- 2) Microcracks initiate from fiber ends by a crazing process (Figure 17).
- 3) The shear rupture is produced either from the fiber pull-out process in a ductile zone or from the macroscopic change (not shown) of crack path along the zig-zag pattern in a brittle zone.
- 4) The ductile-to-brittle transition coincides broadly with slow to fast crack propagation.

The stress-rupture of a typical T-specimen is revealed in the micrographs of Figure 18. A ductile-to-brittle transition is also seen and the fiber debonding (and also the occasional fiber pull-out by the non-ideal situation of fiber orientation) is generally cohesive. Here, "cohesive" debonding is taken to mean that the residual matrix phase adheres to the fiber surface. The word "adhesive" means that there is no residual matrix phase on fiber surface. The fracture surface is mainly through the matrix phase, partially through the interfacially debonded or pulled-out fibers. This corresponds with the two-dimensional, external surface crack propagation studies described above.



10 μ m

Figure 17. Magnified view of notch area of Figure 16.
Cracks start from fiber ends (arrow).

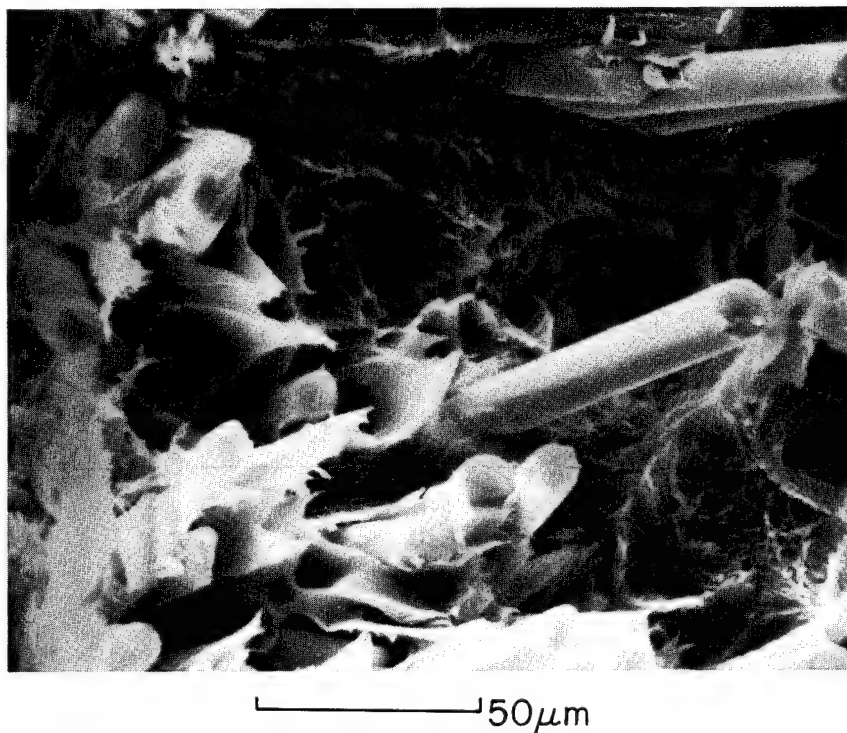


Figure 18. (a) Notch area of stress-rupture L-sample (magnified).

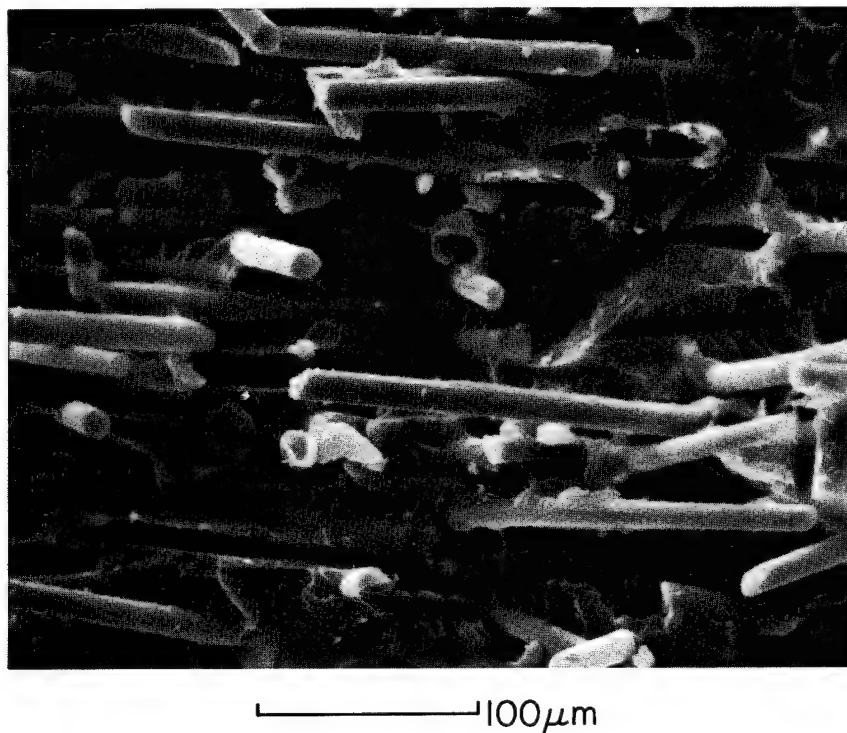


Figure 18. (b) Brittle zone.

2) Constant Strain Deformation and Fatigue

Impact behavior was mimicked by rapid constant strain rate tensile loading, leading to rupture in less than one second. Figure 19 is representative of fracture surface observations on such quasi-impact tests. Long lengths of fiber are pulled out of the matrix. In this case, the fiber debonded and the matrix has flowed plastically as the fibers pulled out of their sockets.

The behavior in constant load amplitude fatigue is considerably different. For both L- and T-orientation, the initial matrix failure is planar and apparently brittle. At a later stage, the matrix fails ductilely. Equally significantly, there are no long lengths of fiber pulled out, but rather the fiber activity is characterized by massive fracture and short pull-out lengths. An example from the transition region between brittle and ductile zones is shown as Figure 20.

It is likely that the fatigue is strongly related to the quasi-impact behavior. A plausible scenario is that debonding and some fiber pullout occur near the crack tip during the tension stroke. On the reverse stroke the fiber can buckle and fracture brittlely. The absence of extensive fiber pull-out and the massive fiber fracture are thereby explained. Possibly the initial apparently brittle failure

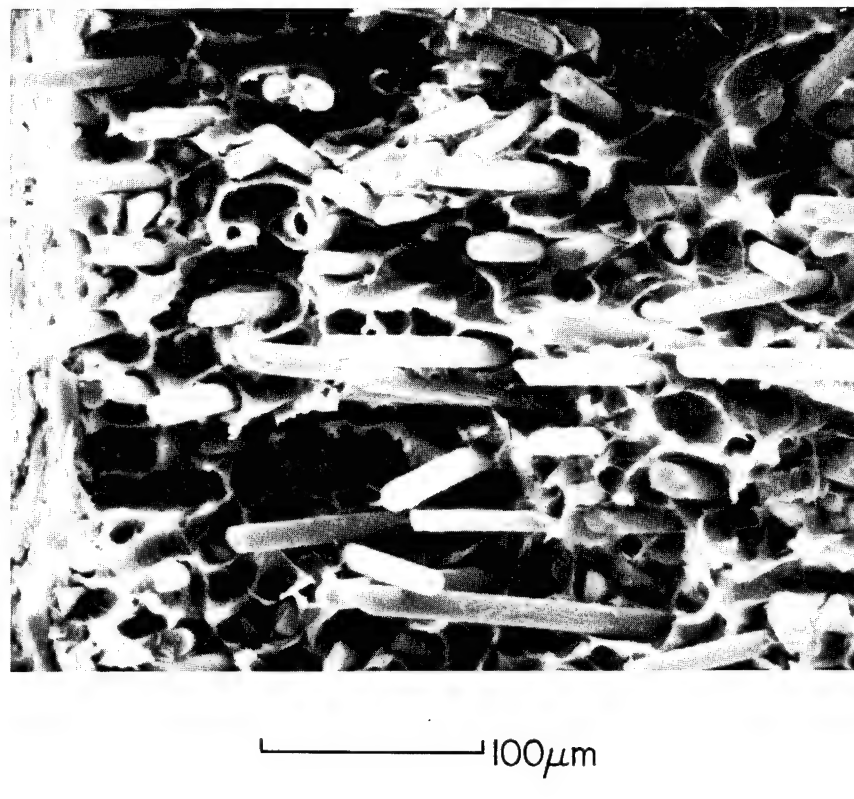


Figure 19. Quasi-impact (constant strain rate)
L-specimen.

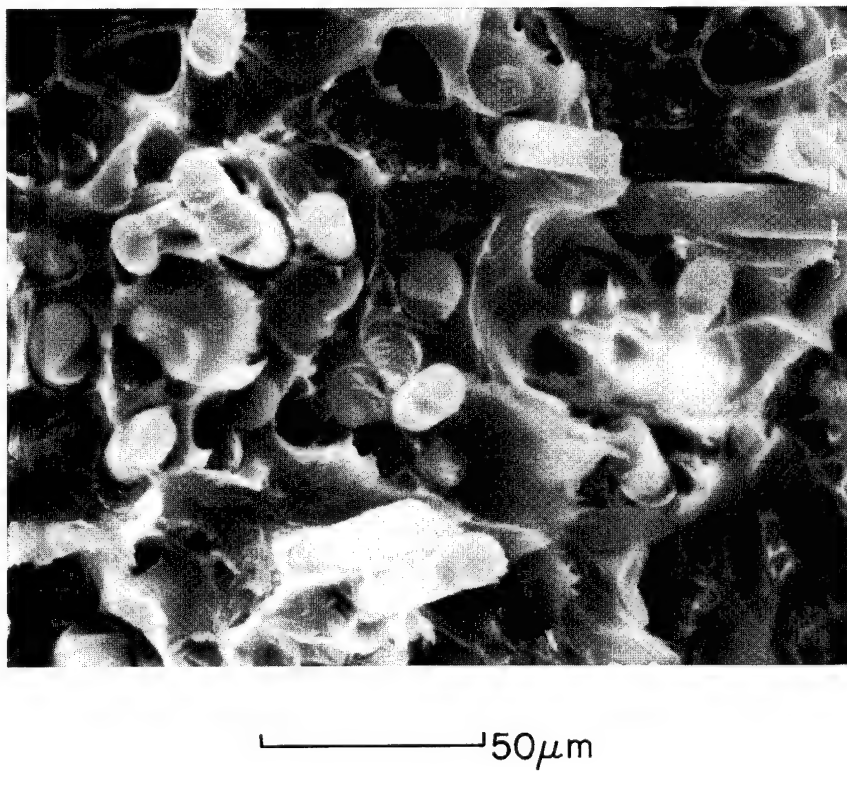


Figure 20. High-cycle fatigue fracture surface, taken from the zone of transition between brittle and ductile behavior.

of the matrix is related to the planarity of the fiber fracture; when a fiber fractures near the crack tip, the stress is locally raised and the failure proceeds along the plane of the fiber fracture. This should occur as long as the mean stress is not high enough to produce microcracking in the far field. When far-field microcracking occurs, the crack is led out of its plane, in order to join the microcracks. Matrix deformation and flow become an important part of this latter behavior.

C. Stress-Rupture Lifetime

The stress intensity-factor equation for compact tension specimens can be presented in the form [21]:

$$K_C = \frac{P}{B\sqrt{a}} f\left(\frac{a}{w}\right) \quad (1)$$

where P is the applied load, B is the specimen thickness, and $f\left(\frac{a}{w}\right)$ is a measure of the compliance of the specimen. K_C is defined as the value of the stress intensity factor K_I at which a crack in the specimen begins to grow before being arrested. Such a K_C is of a macroscopic nature, based on a homogeneous and isotropic material.

The lifetime data of single layer specimens are given in Figure 21 for three fiber orientations. There is a wide

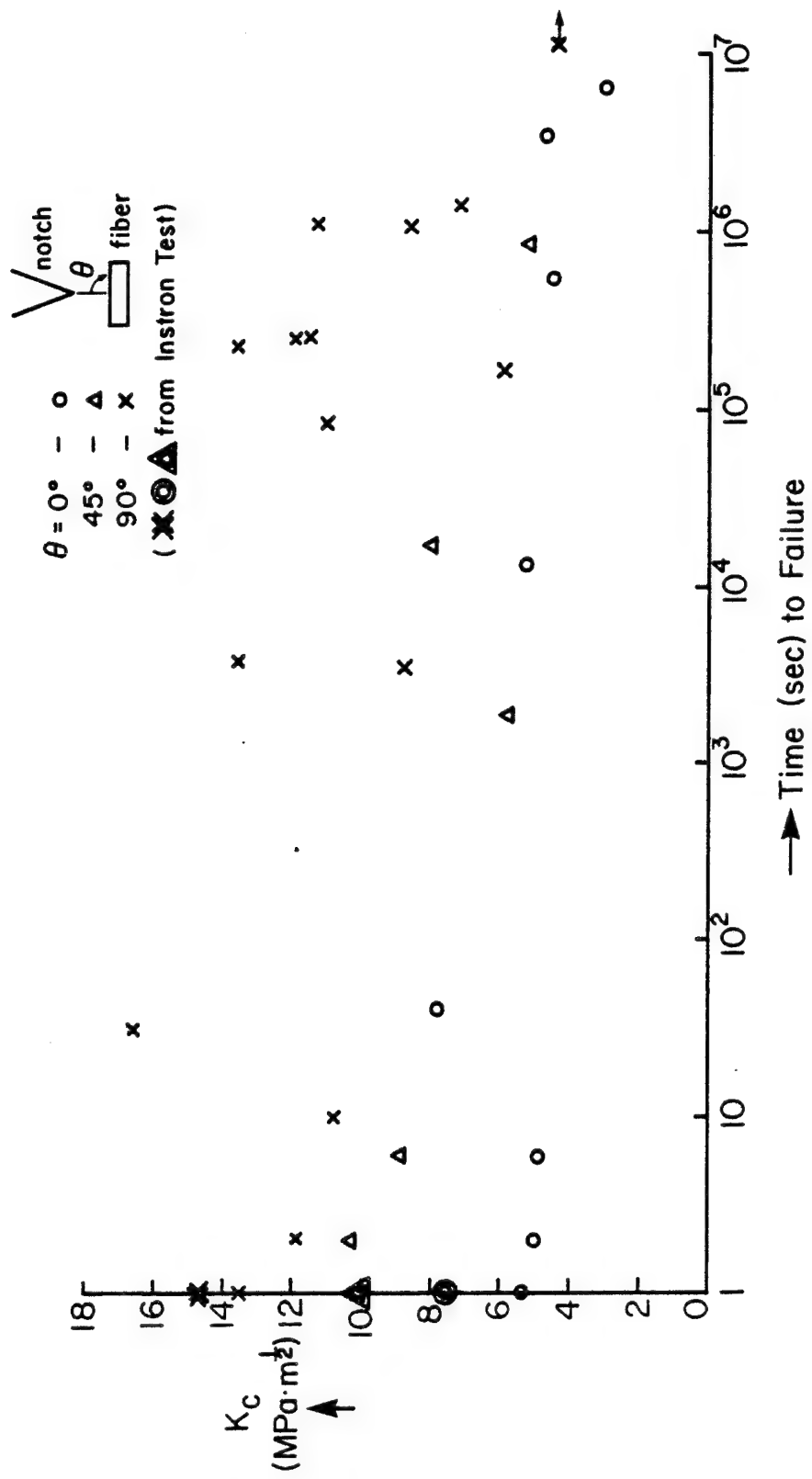


Figure 21. Initial stress intensity - time to failure data of transverse ($x \equiv 90^\circ$), longitudinal ($0 \equiv 0^\circ$), and oblique ($\Delta \equiv 45^\circ$) specimens of single layer.

span of data points and the slope of the data band is very weak. That is, the lifetime is nearly independent of the stress intensity at the crack tip. Data for as-molded, three-ply laminates, shown in Figure 22, exhibits the same type of behavior; lifetimes at a given stress intensity factor are highly spread and there is only weak slope to the data. These results parallel the crack propagation result, in which the crack velocity was also found to be independent of the stress intensity at the crack tip.

Previously, the span of lifetime data was explained by a statistical failure model based on a modified Arrhenius equation [22] and on the linear damage theory [23]. The rate process approach to fracture theory is based on the idea that the breakage of primary (chemical) bonds is thermally activated and time dependent. It has been shown that time-dependent failure plays an important role in polymers and metals. Such a linear damage theory based on this assumption may be applicable to the case of matrix fracture. Fiber fracture is believed to be nearly instantaneous. In the present case, the insensitivity of lifetime to the crack tip stress intensity factor, K_I , is another indication that microfracture far from the crack tip is paramount and that the statistical distribution of flaws and chain ends controls the fracture life.

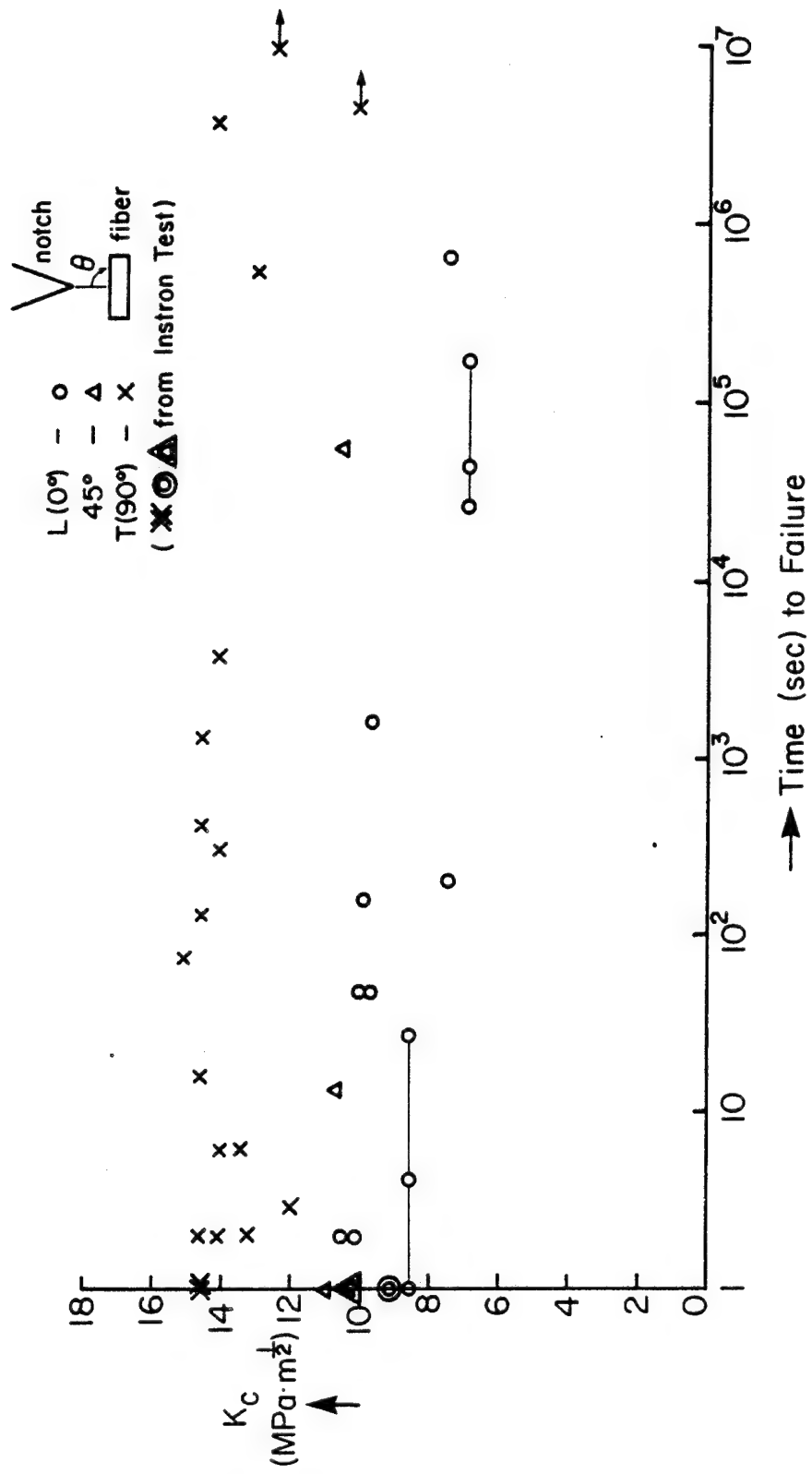


Figure 22. K_c - t_F data of as-molded triple layer (1/16 inch thick).

There may be several reasons for a wide span of lifetime data:

- 1) The variation of specimen thickness from sample to sample (40 mils \pm 5 mils)
- 2) The elimination of internal molded-in stresses during machining causes a very slight warpage of specimen, even though the specimen size is reduced to remove this effect.
- 3) The fiber orientation is not ideal and sometimes quite random locally.

These factors appear to produce a scatter in the K_c vs. t_F data.

D. Tensile Testing and K_c Measurement

Tensile tests were performed on dog bone tensile bars, at a crosshead displacement rate of 0.127 cm/min. 0° , 45° and 90° orientations of fiber axes with respect to the tensile axis were used. Pure resin was also tested. The composites exhibited little or no nonlinearity prior to failure. The resin itself showed an upper yield point and a large degree of plastic flow before failure.

The failure stresses σ_c of the composites are essentially the stresses σ_f of the fiber, because of the low strength and ductility of the matrix. The fiber stresses at failure are the following:

$$(\sigma_f)_L = 191.3 \text{ MPa}$$

$$(\sigma_f)_{45^\circ} = 93.7$$

$$(\sigma_f)_T = 68.5$$

Using Hooke's law, the tensile moduli of the three orientations are:

$$(E)_L = 31.02 \text{ GPa}$$

$$(E)_{45^\circ} = 13.71$$

$$(E)_T = 13.69$$

K_c data for constant strain-rate loading are obtained from the maxima in load-displacement curves of notched compact tension specimens. Results of such tests yield the following results:

$$(K_c)_L^{\text{exper.}} = 14.5 \text{ MPa(m)}^{\frac{1}{2}}$$

$$(K_c)_{45^\circ}^{\text{exper.}} = 9.9 \text{ MPa(m)}^{\frac{1}{2}}$$

$$(K_c)_T^{\text{exper.}} = 7.7 \text{ MPa(m)}^{\frac{1}{2}}$$

The $(K_c)_L^{\text{exper.}}$ will later be compared to a value predicted on a microscopic model. For reference, the strain at composite failure is determined to be:

$$(\varepsilon)_L = 0.0061$$

$$(\varepsilon)_{45} = 0.0068$$

$$(\varepsilon)_T = 0.005$$

DISCUSSION

A. Fractographic Model

A short-fiber composite has many crack initiators, located chiefly at each fiber end. During the period of stress application, the stress concentration at each fiber end, as well as at the notch tip, causes fine microcracks to develop throughout the large volume of the composite. This effect is stronger near the main crack tip than in the remote areas.

When the main crack reaches a fiber, it can either pass through (fiber fracture) or go around (interface fracture). In reality, it follows the fiber/matrix interface, unless there happens to be a fiber fracture induced by a neighboring fiber end long before the main crack tip arrives.

Since the previous interface fracture is not usually complete, the crack grows along the interface until it meets the fiber tip, where it jumps to the end of another previously-developed crack (matrix fracture). But the matrix phase is soft and ductile. Therefore under high load, the matrix crack grows quite rapidly to the next barrier (fiber) and repeats the process of interface fracture.

There are three incidents happening quite far from the main crack tip:

- 1) Fiber breakage induced locally by the combined action of normal and shear stresses.
- 2) Matrix cracking by crazing from numerous fiber ends or broken fiber sections.
- 3) Partial debonding of the matrix/fiber interface.

All three phenomena can contribute to the propagation of the main crack tip by ultimately connecting to the main crack through weak paths. These three modes are observed to occur far in advance of the main crack; they are induced largely by the general stress and are not significantly affected by the stress concentration near the crack tip. Such dispersed microdamage phenomena may therefore be termed far-field. Not all microdamage ultimately becomes connected to the main crack; in some cases there may be local connections between microflaws, with those "branches" leading nowhere. The complexity of the microstructure exhibits itself as a branchy aspect of crack propagation and localized far-field effects.

This is a topological breakdown, characterized by the complexity of cooperative interactions. Stress is not only concentrated at the main crack tip, but also at numerous

fiber ends. Topological breakdown is nothing else than a connecting-up of the pre-existing microcracks along weak paths. This connecting action is also largely a far-field effect, and is only secondarily affected by the immediate field near the main crack tip. The models of far-field effects for L- and T-specimens are illustrated in Figures 23 and 24, respectively.

The mode of final mechanical breakdown is an instantaneous catastrophe in the case of the L-configuration. Initially, the crack grows discontinuously, making numerous branches that are locally separate from each other. The locality of stress singularities induces a competition from various microcracks to join the main crack tip. A weakest path, determined by flaws and cooperative interactions, develops mainly along the interface and matrix. The applied stress is distributed among various crack branches, weakening a stress concentration on the main crack tip. As the crack grows by far-field effects, the stress concentration at the main crack tip reaches a value sufficient to cause an instantaneous fiber pull-out, fiber fracture, and matrix breakage. Prior to breakdown, a crack acceleration is not found (on a very short time duration), since the increase of local stress at the crack is not of large importance.

In the case of an L-specimen, the mode of breakdown is matrix-dominated and crack acceleration can evolve. Partial

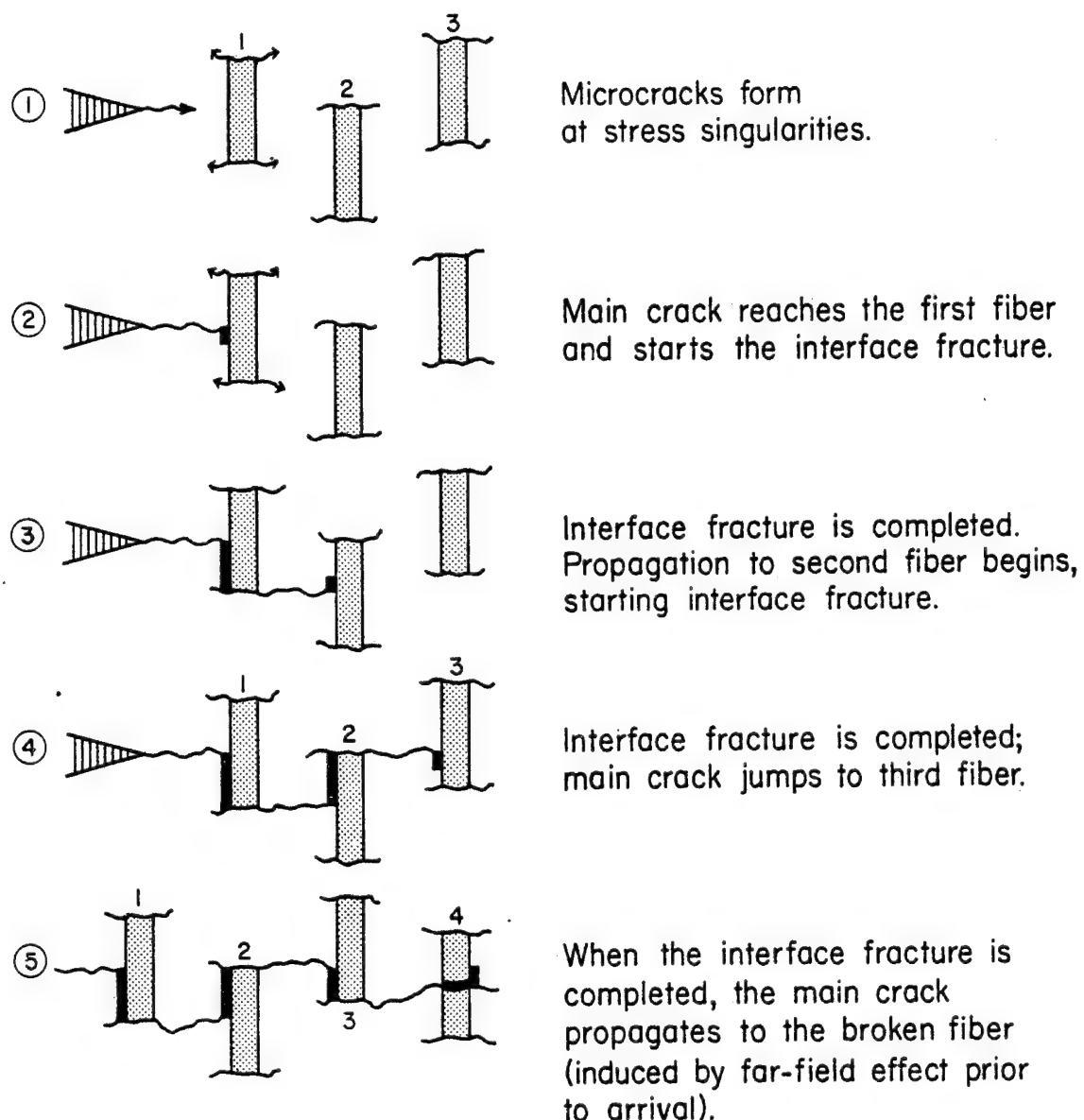
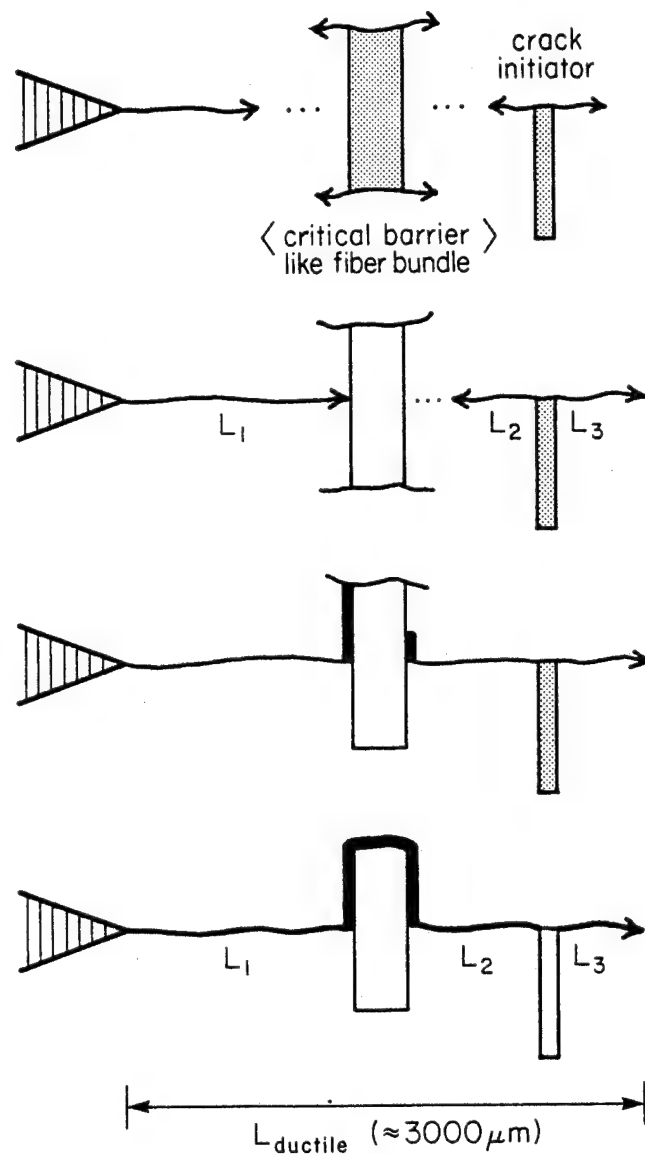


Figure 23. (a) Far-field effect of L-specimen.



Discrete cracks are eventually joined (connected) through the critical barrier, so that the total crack length ($L_1 + L_2 + L_3$) becomes the length of L_{ductile} . At this moment, the material breaks down.

Figure 23. (b) Critical damage induced by far-field effect.

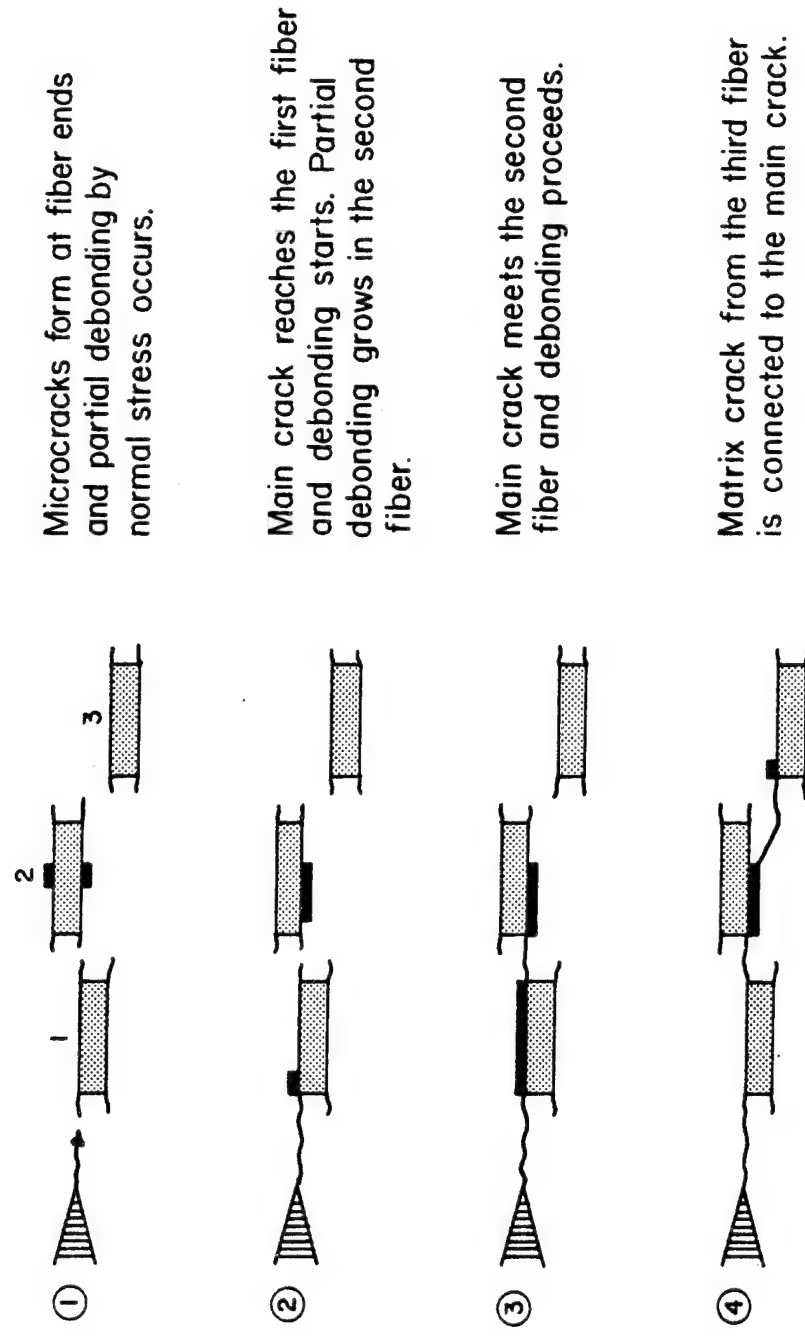


Figure 24. Far-field effect of a T-specimen.

debonding is accomplished by a far-field effect, before the main crack arrives, and therefore the connection of microcracks is done mainly through the matrix phase, secondarily by debonding.

So, the emerging fractographic model proposed in Figure 25 has the following characteristics:

- 1) Weakening of the role of the stress concentration at the main crack tip.
- 2) Unpredictability of crack acceleration to final breakdown.
- 3) Discontinuous (step-wise) mode of crack growth through the far-field effect.
- 4) Apparent crack arrest at a local barrier.
- 5) The time duration of the crack acceleration stage is extremely short, sometimes instantaneous.
- 6) The process of time dependence comes from the interfacial debonding and apparent crack arrest.
- 7) Cracks are propagating in both forward and backward directions.
- 8) Cracks are connected through a weak path and the

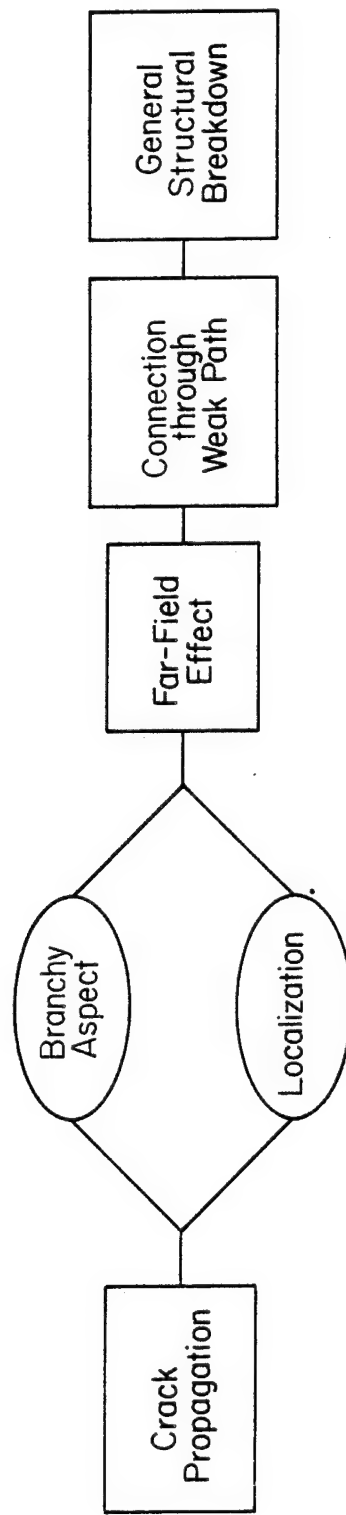


Figure 25. Fractographic model of failure.

far-field zone is advanced. The far-field effect builds up again up to the saturation point where it jumps to the next zone.

B. Microscopic/Macroscopic Correlation

For constant strain-rate testing of L-oriented specimens (fibers parallel to testing axis), it is possible to compute the magnitudes of the several contributions --- fiber fracture, fiber debonding, fiber pull-out, and matrix fracture --- to the work of fracture, W . The sum of these contributions can be compared to the observed total work of fracture, obtained from the stress intensity factor at failure, K_c , and the measured tensile modulus.

Microscopic modeling yields the following for the several contributions to the work of fracture:

- 1) Fiber Fracture Energy, W_f [24]

$$W_f = \frac{\pi d^2 \sigma_f^2 \ell_p}{6E_f} N_f \quad (2)$$

- 2) Fiber Debonding Energy, W_d [25]

$$W_d = \frac{\pi d^2 \sigma_f^2 \ell_p}{4E_f} N_p \quad (3)$$

3) Fiber Pull-Out Energy, w_p [26]

$$w_p = \frac{\pi d^2 \sigma_f^2 \ell_p}{24} N_p \quad (4)$$

4) Matrix Fracture Energy, w_m [27]

$$w_m = \sigma_m \varepsilon_m d [(1 - v_f)^2 / v_f] \quad (5)$$

For the above equations, Table 1 lists the definitions of the parameters, their magnitudes, and the source of the magnitude evaluation. The energy contributions computed from (2) - (5) are:

$$w_f = 0.4 \times 10^{-3} \text{ kg/mm}$$

$$w_d = 1.3 \times 10^{-3} \text{ kg/mm}$$

$$w_p = 478 \times 10^{-3} \text{ kg/mm}$$

$$w_m = 0.6 \times 10^{-3} \text{ kg/mm}$$

The overwhelmingly dominant process is fiber pull-out.

The relationship between the critical stress intensity factor K_c and the total work of fracture W is

$$K_c^2 = WE 2(w_f + w_d + w_p + w_m)E \quad (6)$$

where E is the composite modulus. The value of E obtained in

Table 1. Parameters in Work
of Fracture Equations

<u>Parameter</u>	<u>Definition</u>	<u>Magnitude</u>	<u>Source</u>
d	fiber diameter	12 μm	direct microscopic measurement
σ_f	composite stress at fiber failure	191.3 MPa	tensile test
l_p	maximum pulled-out length of fiber	500 μm	direct microscopic measurement (Fig. 26)
E_f	fiber modulus	72.4 GPa	Ref. [29]
N_f	number of fibers fractured per unit area	306 mm^{-2}	direct microscopic measurement
σ_d	debonding stress; $\sigma_d \approx \sigma_f$	191.3 MPa	tensile test
l_d	average debonded length; same as average pullout length	200 μm	direct microscopic measurement
N_p	number of fibers pulled out per unit area	2614 mm^{-2}	direct microscopic measurement
σ_m	matrix stress at failure	62.5 MPa	Ref. [28]
ε_m	matrix strain at failure	0.0061	tensile test
v_f	volume fraction fibers	0.33	from calculation

tensile tests was 31 GPa. Inserting values for the work and modulus terms in (6), the value of $11.9 \text{ MPa(m)}^{\frac{1}{2}}$ is obtained. This is in reasonable agreement with the value of $14.5 \text{ MPa(m)}^{\frac{1}{2}}$ found by tensile testing of compact tensile specimens. This agreement lends confidence to the acceptance of the individual magnitudes of W_f , W_d , W_p , and W_m .

The dominance of the fiber pull-out mechanism found in relatively rapid constant strain-rate testing will not necessarily extrapolate to loading modes in which either (a) the matrix is given time to flow to eliminate local stress concentrations or (b) the fibers are put into compression over some unsupported length. In the former case, matrix crazing and rupture can supercede fiber pull-out. This change of mode is observed in dead-weight loading. In the latter case, buckled fibers can fracture in the unsupported length. This is likely the case in fatigue loading. There a fiber may partially pull out in the tensile stroke and may buckle in the compression stroke. The massive fiber fracture observed in high-cycle fatigue fracture surfaces is evidence for this mechanism. The distribution of fiber pull-out length is illustrated in Figure 26 for the case of an L-specimen where the maximum pull-out length is estimated to be approximately 500 μm .

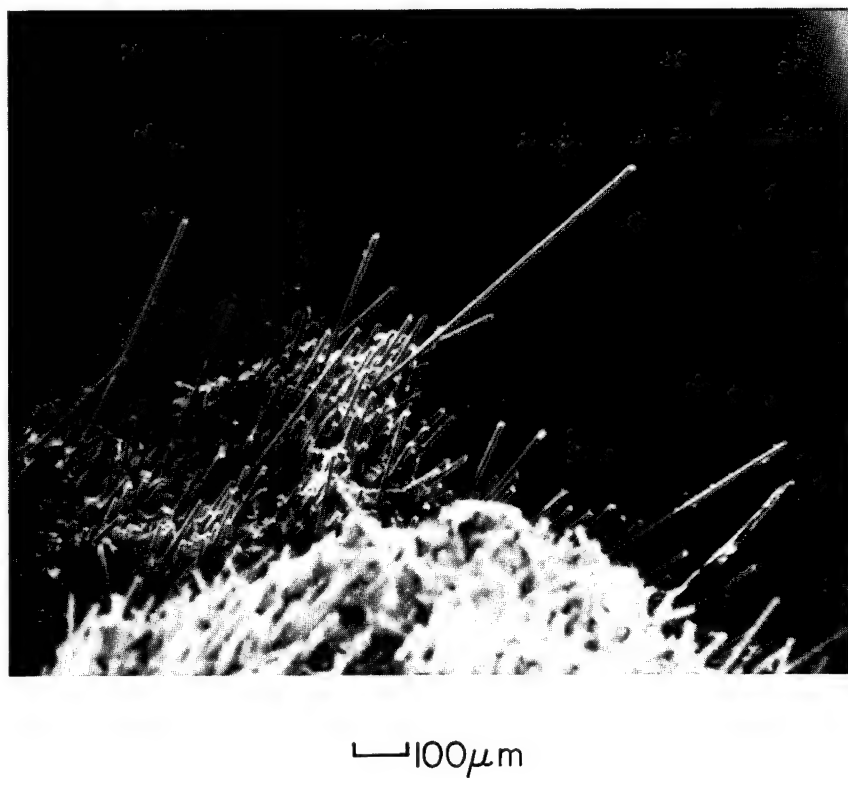


Figure 26. Distribution of fiber pull out-length for L-specimen under 65° tilting. 100 μm scale is visible in the upper part of SEM picture. The maximum pull-out length is estimated to be approximately 500 μm .

CONCLUSIONS

The microscopy and fracture mechanics approach to thermoplastic (PET) reinforced with E-glass short fiber revealed the following points:

- 1) In dead-loading and constant strain-rate loading, the crack propagates along the fiber/matrix interface and the matrix phase, the critical step being the interfacial fracture.
- 2) There is a sudden breakdown accomplished by the topological connection through a weak path. The part-through breakdown occurs when the modification of the effective notch geometry by the damage zone is such that sequential failure is self-catalyzed; i.e., the stress gradient ahead of the incipient crack must be such that crack propagation can be self-sustaining.
- 3) The fiber fracture and microcracks from fiber ends are induced by a far-field effect, not by an immediate field near the crack tip.
- 4) There is a ductile-to-brittle transition of the

matrix phase in stress-ruptured specimens from the notch to the other end. The velocity of crack propagation is related to this transitional behavior; i.e., the slow crack propagation correlates to a ductile mode and fast propagation correlates to a brittle mode.

- 5) In fatigue experiments, the transitional behavior is from brittle to ductile mode. The brittle fracture behavior is likely due to buckling fracture of partially pulled-out fibers.
- 6) Impact (or quasi-impact) causes a massive fiber pull-out, while fatigue causes a massive fiber fracture. Both are present in stress-rupture tests.
- 7) There are two bounds (lower and upper) on stress-rupture lifetime and in between these two bounds the load vs. lifetime data has a wide span with a very weak slope.
- 8) The lifetime of the L-configuration is higher than both T- and 45°-configurations. This is due to the additional fiber pull-out energy for fracture in the case of L-specimens. The fracture of

T- and 45°-specimens occurs mainly by matrix cracking plus partial interface debonding.

- 9) Fiber fracture away from the crack tip zone is aided by the shear stress induced by a neighboring fiber end.
- 10) The dominant process in the work of fracture for constant strain-rate loading is fiber pull-out. It appears that this dominance does not extend to stress rupture or to high-cycle fatigue loading.

REFERENCES

1. K. Friedrich, "Microstructure and Fracture of Fiber Reinforced Thermoplastic Polyethylene Terephthalate (Rynite ®)," Report CCM-80-17, Center for Composite Materials, University of Delaware, 1980.
2. K. Friedrich, Praktische Metallographie, 1980.
3. K. Friedrich, Kunststoffe, 1981.
4. Jean C. Malzahn, M.Ch.E. Thesis, Univ. of Delaware, 1982.
5. J. O. Outwater and M. C. Murphy, 24th Ann. Tech. Conf. Society of Plastics Ind. (1969) 1.
6. G. A. Cooper and A. Kelly, J. Mech. Phys. Sol. 15 (1967) 279.
7. C. Zweben, J. Mech. Phys. Sol. 19(1971) 103.
8. E. M. Wu, Comp. Mat. Workshop, Technomic Publishing Co., Inc. (1968) 20.
9. H. J. Konish et al., J. Comp. Mat. 6(1972) 114.
10. M. J. Owen and P. T. Bishop, J. Comp. Mat. 7 (1973) 146.
11. C. D. Ellis and B. H. Harris, J. Comp. Mat. 7(1973) 76.
12. P. W. Beaumont and D. C. Phillips, J. Mater. Sci. 7(1972) 682.
13. J. F. Mandell et al., "Eng. Aspects of Fracture Toughness: Fiber Reinforced Laminates," 29th Ann. Tech. Conf. Society of Plastics Ind. 17-D (1974) 1.
14. S. Gaggar and L. J. Broutman, ASTM STP 631 (1977) 310.
15. P. T. Curtis, M. G. Bader and T. F. Bailey, J. Mater. Sci. 13(1978) 377.
16. M. G. Bader, T. W. Chou and J. Quigley, "New Developments

- and Applications in Composites," edited by D. Wildsdorf, The Metallurgical Soc.--AIME, N.Y. 1979.
17. H. Fukuda and T. W. Chou, J. Mater. Sci. 16(1981) 1088.
 18. C. Lhymn, M.S. Thesis, Univ. of Delaware (1982).
 19. E. Baer, "Polymeric Materials," ASM, Metals Park, Ohio (1975).
 20. A. T. Dibenedetto et al., Polym. Eng. and Sci. 19(1979) 345.
 21. S. T. Rolfe, Fracture and Fatigue Control in Structures, Prentice Hall, Inc., Englewood Cliffs, New Jersey (1977).
 22. C. C. Chino et al., J. Comp. Mat. 11(1977) 79.
 23. J. M. Schultz, Treatise on Materials Science and Technology. Vol. 10. Properties of Solid Polymeric Materials, J. M. Schultz, ed., Academic Press, New York (1977) p. 599.
 24. J. FitzRandolph, D. C. Phillips, P. W. R. Beaumont, A. S. Tetelman, J. Mater. Sci. 7(1972) 289.
 25. D. H. Kaelble, J. Adhesion 5(1973) 245.
 26. J. K. Wells and P. W. R. Beaumont, J. Mater. Sci. (1982) 397.
 27. G. A. Cooper and A. Kelly, J. Mech. Phys. Solids 15(1967) 279.
 28. K. M. Gupte, Ph.D. Dissertation (1981) Univ. of Delaware.
 29. G. Lubin, Handbook of Composites, Van Nostrand Reinhold Company (1982).

APPENDIX

Failure Mode of Artificial Laminates

The lamination was accomplished by the following processes:

- 1) Rough-polish the surface (#600 emery paper).
- 2) Clean the surface with acetone.
- 3) Use a special film adhesive (FM300M, 10 mils thick) between plies.
- 4) Stack the specimen laminae in a metal mold.
- 5) Curing condition: ($180^{\circ}\text{C}/\text{a>r}/\sim 100 \text{ psi}/3 \text{ sec}$).
Heat up to 180°C under pressure and then slowly cool down to room temperature still under pressure.
- 6) Separate the laminated specimen from the metal mold.

High temperature curing ($\geq 250^{\circ}\text{C}$) above the melting point of the matrix phase ($\sim 240^{\circ}\text{C}$) produces an intimate bonding between each lamina, but the strength degrades severely, affecting the fracture toughness (K_c : stress intensity factor

of the laminate. The microstructure of a fractured surface of the specimen which has undergone high temperature curing reveals a poorly bonded interface between the fiber and matrix, believed to be caused by deteriorated coupling agent.

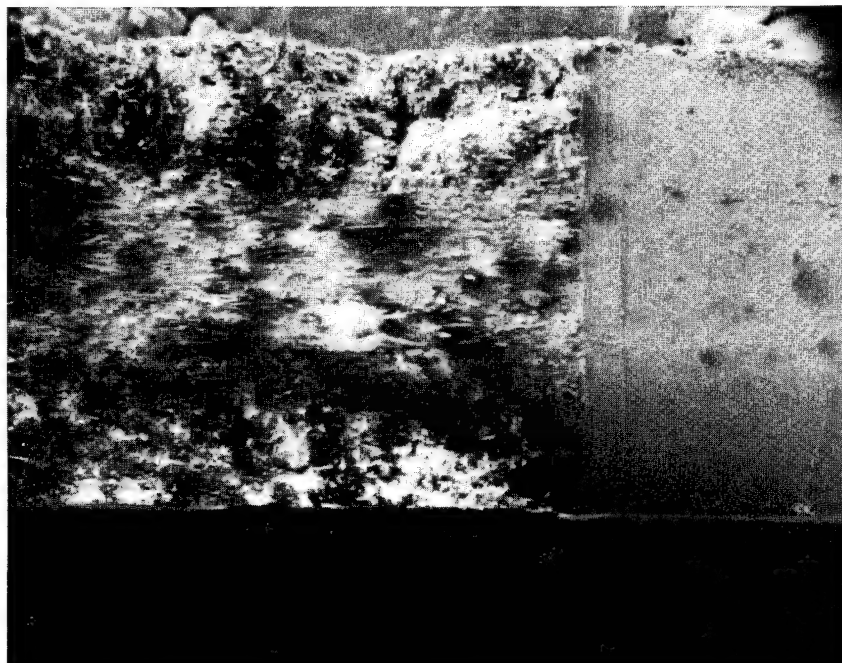
Two kinds of fracture mode are distinguished:

- 1) Type A (delamination mode)
- 2) Type B (intimate mode)

The type A mode is characterized by partial or complete delamination along the interface between two plies. Each layer has its own characteristic fracture aspect, independent of the presence of the neighboring ply. The matrix phase is not continuous across the boundary but is delaminated locally. In this case, the shear force along the boundary is greater than the adhesive bonding force.

The type B mode shows an intimate continuity of the matrix phase at the boundary zone. The fracture aspects are cooperative and there is no delamination. In this mode, the shear force along the boundary is less than the adhesive bonding.

The (T/L/T) laminates are shown in Figures A-1 and A-2 for type B and A respectively. Sometimes the delaminated zone reveals a secondary crack, as shown in Figure A-2. This



— 800 μ m

Figure A-1. (T/L/T) laminate showing type B mode.



— 800 μ m

Figure A-2. (90°/0°/90°) laminate showing type A mode.

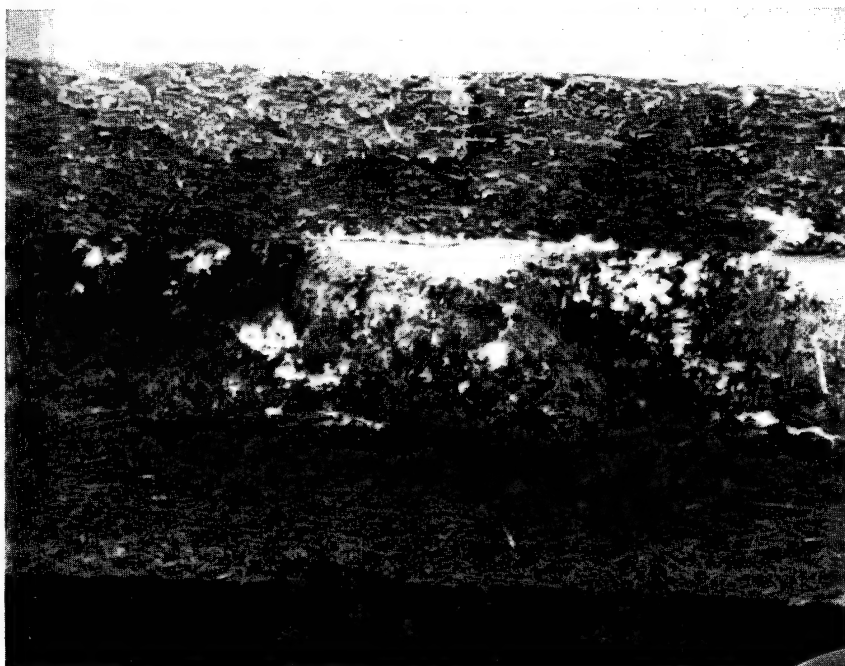
is believed to occur when the difference between the shear and adhesive force is very little.

The (L/T/L) laminate is shown in Figure A-3. A locally magnified area of Figure A-3 is shown in Figure A-4.

Either type A or type B mode occurs in both (T/L/T) and (L/T/L) laminates. The controlling factor appears to be a curing temperature and the residual stress of each ply.

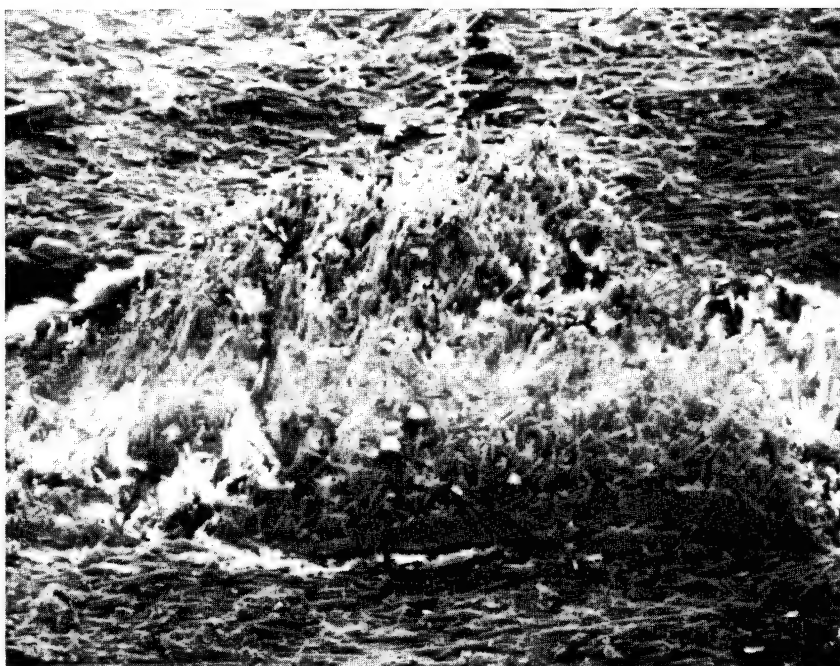
The (+45°/0°/-45°) laminate shown in Figure A-5 reveals a type A mode, where both (+45°) and (-45°) ply tend to merge together as the crack propagates (favorable-to-unfavorable transition). At a locally unfavorable spot along (+45°) ply, the severe shear rupture is seen in Figure A-6. The (+45°/-45°) laminate always shows the type A mode as in Figure A-7. The (90°/0°) laminate develops type A or Type B fracture mode. The non-ideal fiber orientation is vividly demonstrated in Figure A-8 for the (90°/0°) laminate. The lifetime vs. initial load data are shown in Figure A-9.

The (90°/0°/90°) laminate shows the highest K_C value, the 90° layer contributing a significant portion to a high K_C . In the process of artificial lamination, the curing temperature is the critical factor. Thermal bonding without film adhesive turns out to be unsuccessful because of the specimen collapse caused by the matrix fluidity at a high temperature.



800 μ m

Figure A-3. (0°/90°/0°) laminate.



800 μ m

Figure A-4. Local zone of Figure A-3.

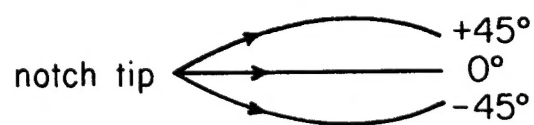
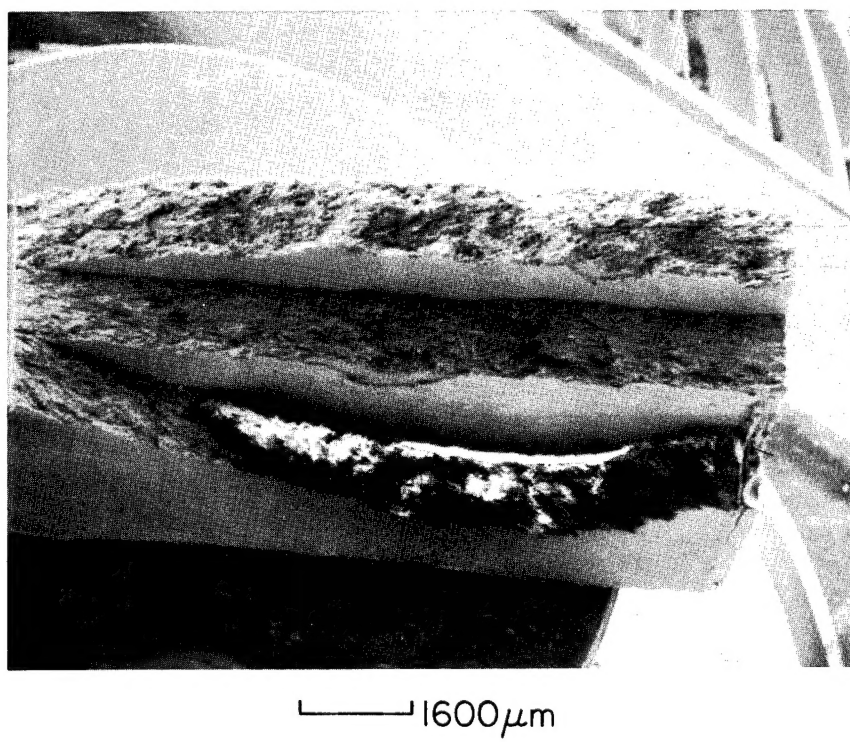
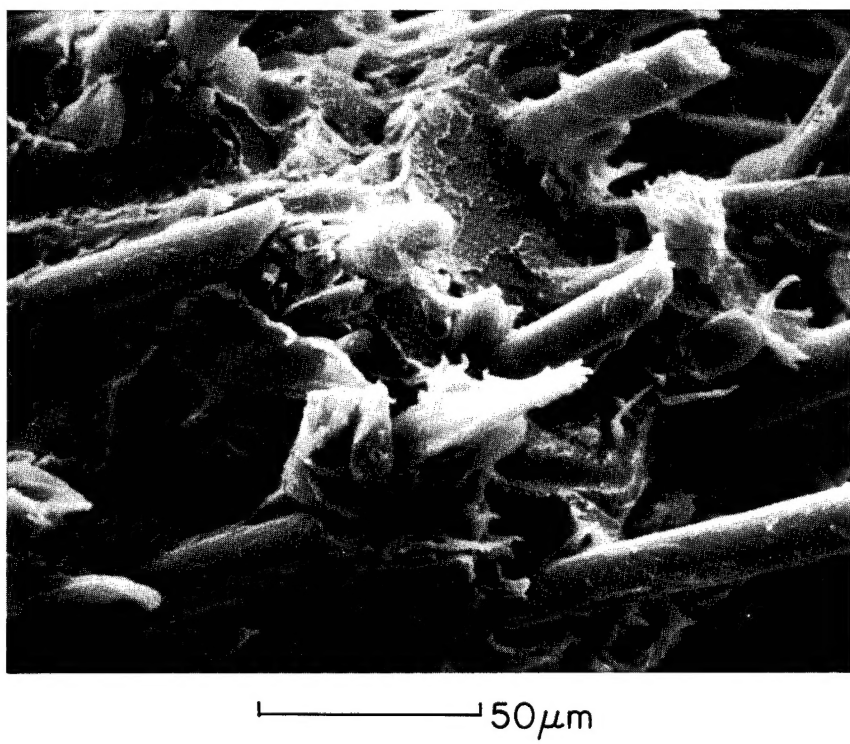


Figure A-5. The $(+45^\circ/0^\circ/-45^\circ)$ laminate.



50 μm

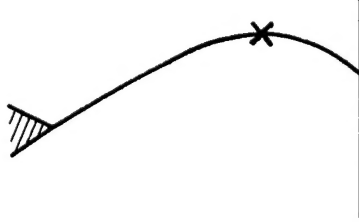
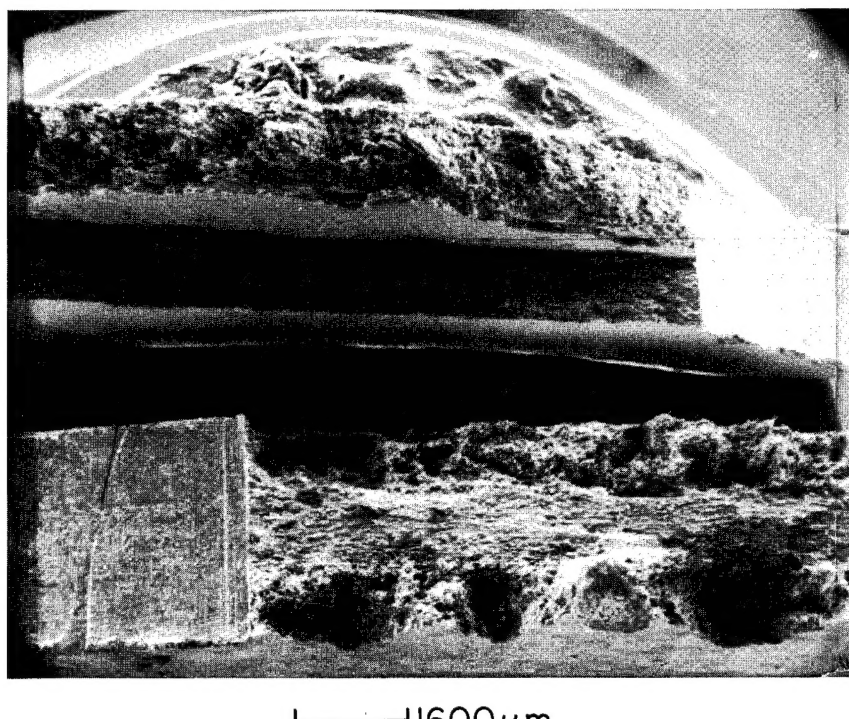
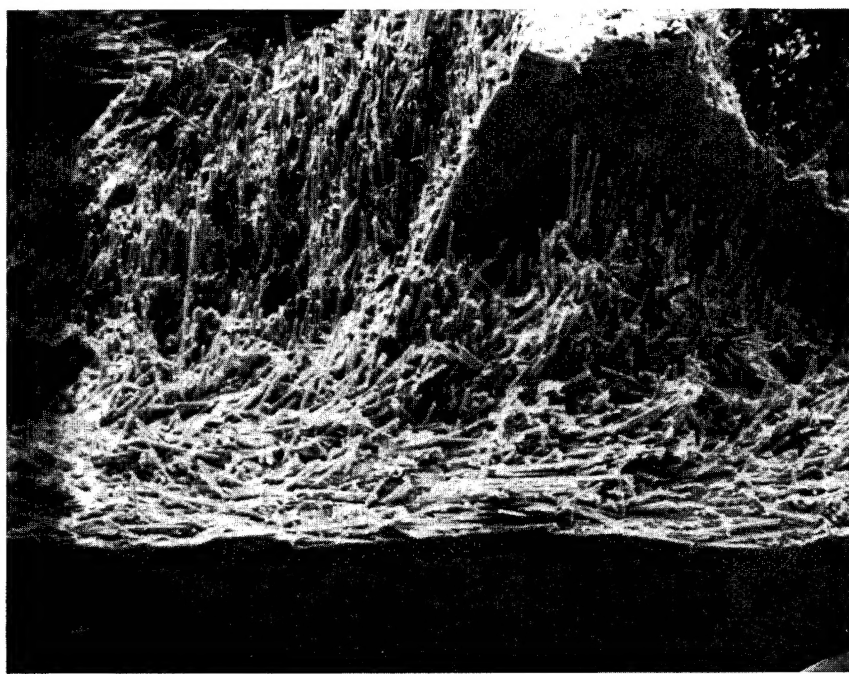


Figure A-6. The locally unfavorable spot along ($+45^\circ$) ply.



1600 μ m

Figure A-7. The (+45°/-45°) laminate.



400 μ m

Figure A-8. The (90°/0°) laminate.

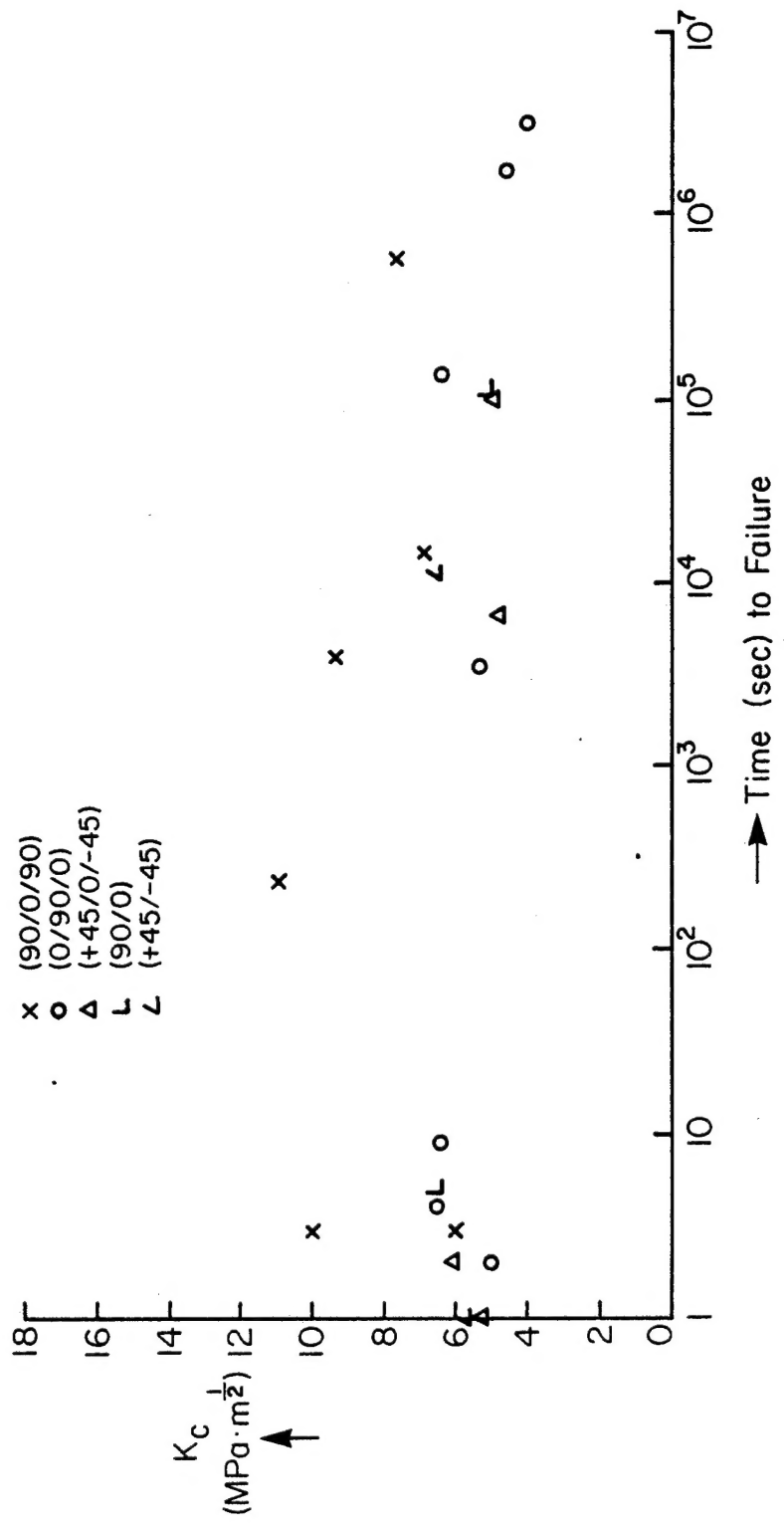


Figure A-9. K_c vs. lifetime data for artificial laminates.